One-Sentence Summary: Protein transfer through matrix-bound vesicles from cancer-associated fibroblasts enhances monocyte adhesion to endothelial cells.

Editor's Summary:

Malignant messages to endothelial cells

Cancer-associated fibroblasts promote tumor growth in part by releasing extracellular vesicles, which can carry proteins to cells in the tumor microenvironment. Santi *et al.* investigated intercellular communication between endothelial cells in blood vessels and cancer-associated fibroblasts isolated from patients with breast cancer. Endothelial cells in vitro and in vivo took up proteins from extracellular vesicles, specifically matrix-bound vesicles, released by cancer-associated fibroblasts. Uptake of the membrane glycoprotein THY1 from cancer-associated fibroblasts increased the adhesion of monocytes to endothelial cells. Cancer-associated fibroblasts that released the most matrix-bound vesicles resembled myofibroblasts, thus identifying the proteins released by myofibroblast-like cancer-associated fibroblasts that alter endothelial cell function could yield potential targets for disrupting this intercellular communication.

Cancer-associated fibroblasts produce matrix-bound vesicles that influence endothelial cell function

Alice Santi[1‡], Emily J Kay[1‡], Lisa J Neilson[1], Lynn McGarry[1], Sergio Lilla[1], Margaret Mullin[3], Nikki R Paul[1], Frédéric Fercoq[1], Grigorios Koulouras[1,2], Giovanny Rodriguez Blanco[1], Dimitris Athineos[1], Susan Mason[1], Mark Hughes[1], Gemma Thomson[1], Yann Kieffer[4,5], Colin Nixon[1], Karen Blyth[1,2], Fatima Mechta-Grigoriou[4,5], Leo M Carlin[1,2], Sara Zanivan[1,2,*]

[1]Cancer Research UK Scotland Institute, Glasgow G61 1BD, UK; [2]School of Cancer Sciences, University of Glasgow, Glasgow G61 1QH, UK; [3]College of Medical, Veterinary, and Life Sciences, Institute of Infection, Immunity and Inflammation, University of Glasgow, Glasgow G12 8QQ, UK; [4]Equipe Labellisée Ligue Nationale Contre le Cancer, Institut Curie, PSL Research University, 26, rue d'Ulm, 75005 Paris, France; [5]Inserm, U830, 75005 Paris, France.

‡ These authors contributed equally to this work.

*Corresponding author: Sara Zanivan s.zanivan@beatson.gla.ac.uk

Abstract

Intercellular communication between different cell types in solid tumors contributes to tumor growth and metastatic dissemination. The secretome of cancer-associated fibroblasts (CAFs) plays major roles in these processes. Using human mammary CAFs, we showed that CAFs with a myofibroblast phenotype released extracellular vesicles that transferred proteins to endothelial cells (ECs) that affected their interaction with immune cells. Mass spectrometry-based proteomics identified proteins transferred from CAFs to ECs, which included plasma membrane receptors. Using THY1 as an example of a transferred plasma membrane-bound protein, we showed that CAF-derived proteins increased the adhesion of a monocyte cell line to ECs. CAFs produced high amounts of matrix-bound EVs that were the primary vehicles of protein transfer. Hence, our work paves the way for future studies that investigate how CAF-derived matrix-bound EVs influence tumor pathology by regulating the function of neighboring cancer, stromal, and immune cells.

Introduction

Communication between cells is fundamental for the physiological function of tissues [1, 2] and alterations can cause diseases and determine their severity [3-5]. In solid tumors, intercellular communication involves cancer cells and neighboring cells of the tumor microenvironment (TME) and modulates tumor growth and metastatic dissemination. The TME is a highly heterogeneous and dynamic compartment that comprises pathological and activated immune and stromal cells, which include cancer-associated fibroblasts (CAFs) and endothelial cells (ECs) [6, 7].

CAFs are highly secretory cells and represent the bulk of the stroma of solid tumors with a desmoplastic reaction, such as breast cancer [8, 9], and are thus a considerable source of chemical signals that can affect the behavior of cancer, immune and stromal cells. For these reasons, CAFs have been defined as “architects of cancer pathogenesis” [10] or as “architects of stroma

remodeling" [6]. The repertoire of chemical signals produced by CAFs includes growth factors, cytokines, non-coding RNAs, components of the extracellular matrix (ECM) and ECM remodeling enzymes, which regulate invasion, proliferation and chemoresistance of cancer cells, blood vessel formation and the recruitment and function of immune cells [6, 10-14]. CAFs carry out these different functions by acquiring distinct but interchangeable states [15]. Myofibroblast-like CAFs (myCAFs) and inflammatory CAFs (iCAFs) are the two main subtypes that have been described in tumors, including breast cancer [15, 16]. myCAFs are responsible for ECM production and remodeling and have immunosuppressive functions, whereas iCAFs have an immunomodulatory role [15, 17]. In addition to these mechanisms of paracrine crosstalk, CAFs transfer various nutrients [18-20], proteins, lipids [21, 22] and even entire mitochondria [23, 24] to cancer cells, which use these CAF-derived resources to support their own growth and motility.

The intercellular transfer of cell surface and intracellular proteins has been extensively documented between immune cells. The physiological role and functional consequences of this phenomenon are still unclear, but may help to regulate the immune response [25-29]. So far, few papers have examined the ability of pathologically activated fibroblasts to transfer their own proteins to cancer cells. These papers showed that the transfer of proteins from CAFs to cancer cells occurs through large extracellular vesicles (EVs) that CAFs release in the conditioned medium (CM) and that it supports cancer cell proliferation [21] and migration [22]. There remain several open questions about the protein transfer ability of CAFs. Do other stromal cells also receive CAF-derived proteins? If so, what is the biological relevance of this intercellular protein transfer?

EVs are lipid bilayer-enclosed particles that mediate cell-cell communication by transferring proteins, lipids, and nucleic acids between cells. In accordance with the MISEV guidelines, EVs are classified based on their size as small (diameter <100-200 nm) and medium/large (diameter >150-220 nm) [30]. Medium/large EVs directly bud from the plasma membrane (ectosomes), whereas

small EVs originate from either the endosomal compartment (exosomes) or the plasma membrane (ectosomes) [30, 31]. EVs that transfer biological material between cells are typically found in cell-derived CM (CM-EVs) [14]; however, EVs can be embedded within the ECM of decellularized tissues and of murine NIH-3T3 fibroblast cell cultures [32, 33]. These matrix-bound vesicles (MBVs) have a similar shape and morphology to CM-EVs but differ in lipid and microRNA content [33]. MBVs are biologically active [32, 34]; however, their protein composition and role in intercellular protein transfer have not yet been reported.

Tumor blood vessels are typically embedded within the tumor stroma; therefore, we have investigated whether CAFs employ intercellular protein transfer to influence the function of ECs. Using CAFs isolated from patients with breast cancer as donors and human ECs as recipient cells, we have identified a specific pool of proteins that CAFs transfer to ECs and, using THY1 as example, we provide proof of principle that they can be functional in the ECs. Moreover, we found that CAFs deliver proteins principally through MBVs and that CAFs expressing myCAF markers are the main donors of proteins to ECs.

Results

CAFs transfer proteins to ECs

To study whether mammary CAFs transfer proteins to ECs, we used several CAF lines that we have isolated from patients with breast cancer (pCAFs). These pCAFs express the mesenchymal marker vimentin (fig. S1A) [35], but are negative for markers of epithelial, endothelial and immune cells (fig. S1B). Our lab has previously characterized the pCAF2 and pCAF3 lines [35]. To study the process of protein transfer between cells and its biological relevance, we used different culturing methods (fig. S1C).

To monitor the transfer of proteins from pCAFs (donor cells) to human umbilical vein ECs (HUVECs, recipient cells), we fluorescently labeled the pCAF proteome with CFSE, a dye that covalently binds to amino groups. Microscopy analysis showed that HUVECs became fluorescent after being co-cultured for 24h with CFSE-labeled pCAFs, indicating that pCAFs transferred some of their proteins to HUVECs (Fig. 1A-B and fig. S1D).

Using the same CFSE-based labeling method, we quantified the intercellular transfer of proteins by flow cytometry, which confirmed that HUVECs acquire fluorescent signals upon co-culture with CAFs (Fig. 1A, C-F). Notably, the quantity of transferred proteins depended on the number of donor cells and it increased in accordance with the ratio between pCAFs and ECs (Fig. 1A, C-D). The shift of the CFSE peak of co-cultured HUVECs compared with monoculture showed that the vast majority of the HUVECs received pCAF proteins, indicating that this is a commonly occurring event (Fig. 1A, D). Conversely, HUVECs transferred very low amounts of proteins to pCAFs (Fig. 1A, E) or to other HUVECs (Fig. 1A, F). In addition, pCAFs had a much higher protein transfer ability compared to MDA-MB-231 cells, which are aggressive breast cancer cells (Fig. 1A, F). These results indicate that pCAFs and HUVECs do not mutually exchange proteins and that CAFs are major protein donors.

Once we established that pCAFs transfer proteins to HUVECs in vitro, we sought to assess whether this mechanism also occurred in vivo. For this purpose, we used the C.FVB-tg(Acta2-DsRed)1RK1/J mouse model [36], also known as α-SMA-RFP. This model expressed the red fluorescent protein (RFP) in cells expressing the alpha-smooth muscle actin gene (*Acta2,* whose product is α-SMA protein). Because α-SMA is a widely used CAF marker [7, 15, 37], we used the α-SMA-RFP model to monitor the transfer of RFP from *Acta2*-expressing cells to ECs in experimental pulmonary metastases, as a mean of protein transfer from CAFs to ECs. 4T1 murine breast cancer cells were injected in the tail vein of α-SMA-RFP mice and, after three weeks, we dissected tumor-containing

lungs (fig. S1E) and analyzed single cell suspensions by flow cytometry. We used α-SMA-RFP mice that had not been injected with 4T1 cells as control to measure whether RFP protein could be transferred to the endothelium in the absence of *Acta2*-expressing CAFs (for example by perivascular cells, such as pericytes, which also express *Acta2*). Flow cytometry analysis measured a significant increase of RFP^+ ECs in mice with lung metastases compared with the control (Fig. 1G). To confirm these results, we imaged fixed precision cut lung slices with 4T1 metastases from α-SMA-RFP mice (Fig. 1H). The 3D reconstruction of tumor sections, which were stained for CD31 to visualize ECs, showed RFP^+ endothelium in the lung metastases of these mice (Fig. 1H, I), but not in non-RFP expressing control mice (fig. S1F). Overall, our data provide evidence that CAFs communicate with ECs through the transfer of proteins in vitro and in vivo.

CAFs transfer plasma membrane receptors to ECs

To identify proteins that pCAFs transfer to HUVECs, we used a mass spectrometry (MS)-based trans-stable-isotope labeling of amino acids in cell culture (trans-SILAC) proteomic approach [28]. First, we labeled the proteome of pCAFs with the heavy isotopologue of arginine and lysine, and co-cultured them with unlabeled HUVECs for 4h or 24h. Then, we sorted the HUVECs and analyzed their proteome by MS (Fig. 2A). We quantified 808 and 1062 heavy-labeled proteins in at least three out of five biological replicates at 4h and 24h time points, respectively (Fig. 2B and Data File S1). Of these, 698 proteins were common to both time points (Fig. 2B). Gene Ontology Cellular Component (GOCC) term analysis of the proteins transferred from CAFs to the HUVECs revealed enrichment in lipid bilayer-enclosed vesicles, endoplasmic reticulum (ER), ER-Golgi intermediate compartment, and macromolecular complexes, including focal adhesions, cell junctions, ribonucleoprotein particles and proteasome (Fig. 2C). The high number of common proteins and the consistency of the top ten enriched GO terms between the two time points indicate that there is a continuous transfer of proteins over time from CAFs to ECs in culture. Moreover, the

association of these proteins with particular subcellular compartments suggests that mammary CAFs transfer selected protein subsets.

Cancer and immune cells use EVs to transfer functional plasma membrane proteins to ECs [38, 39]. These types of proteins are highly relevant because they may alter the function of the endothelium, including its interactions with surrounding cells. Therefore, we focused our analysis on plasma membrane receptors and membrane-bound ligands. We found that the majority of the transferred membrane proteins were involved in immune response, cell locomotion, cell-cell and cell-matrix adhesion (Fig. 2D) [40-44], corroborating the idea that CAF-derived proteins may have important implications on the functions of the tumor vasculature. To select for proteins that provided the biggest changes in the HUVEC proteome, we determined the contribution of each transferred protein to the corresponding endogenous protein in the HUVECs and referred to this value as “exogenous fraction”. The exogenous fraction ranges between 0 and 1, and the closer the value is to 1, the more the pCAF protein contributes to the endothelial counterpart (Fig. 2E and Data File S1). CAF-derived Thy-1 (THY1) was the protein with the highest contribution to the HUVEC proteome, with an exogenous fraction of 0.78 and 0.54 after 4h and 24h of co-culture, respectively (Fig. 2E and Data File S1). CD44 antigen (CD44) also contributed highly with an exogenous fraction of 0.46 and 0.35 at 4h and 24h, respectively, and then integrin beta-3 (ITGB3), with an exogenous fraction of 0.21 at 24h of co-culture. The exogenous fraction for all the other receptors and ligands was lower than 0.15 (Fig. 2E and Data File S1). Overall, these results indicate that mammary CAF-derived receptors and ligands can quantitatively modify the proteome of the HUVECs.

CAF-derived THY1 induces functional changes in ECs

To confirm that the THY1 detected in HUVECs was derived from pCAFs, rather than being expressed by HUVECs when co-cultured with them, we measured *THY1* transcript in HUVECs in

monoculture and after 24h of co-culture with pCAFs. Using pCAFs as the control for *THY1* expressing cells, we found that *THY1* mRNA amount did not increase significantly in co-cultured HUVECs compared to the monoculture (Fig. 3A, B). In addition, flow cytometry analysis confirmed the transfer of THY1 from pCAFs to HUVECs (Fig. 3A, C-E). Although THY1 was not present at the surface of HUVECs in monoculture, after 24h of co-culture with pCAFs, the majority of HUVECs positively stained for THY1 (Fig. 3A, D, E). Moreover, pCAFs silenced for THY1 (Fig. 3C) transferred significantly less THY1 to HUVECs (Fig. 3A, D, E), whereas the total amount of transferred proteins was not affected (Fig. 3A, F).

THY1 (also known as CD90) is a glycophosphatidylinositol-anchored protein that localizes on the extracellular side of the plasma membrane of cells and that binds to cancer cells and leukocytes through plasma membrane receptors [45, 46]. In inflammatory disease, the recruitment of immune cells requires their physical interaction with the endothelium mediated by adhesion molecules [47, 48]. THY1 expressed on the endothelium participates in this process by interacting with its binding partners present on the leukocyte surface, such as CD11b (also referred to as integrin alpha-M, ITGAM) [49-51]. To assess the function of pCAF-derived THY1, we measured leukocyte adhesion to HUVECs when co-cultured with pCAFs silenced or not for THY1. Specifically, we used the human monocyte cell line THP-1 that expresses several THY1 binding partners (fig. S2A and Data File S2). Microscopy analysis of the co-cultures showed that significantly fewer monocytes adhered to HUVECs when co-cultured with THY1-silenced pCAFs compared with control co-culture (siCtrl), supporting the functionality of THY1 on the HUVEC surface (Fig. 3A, G and fig. S2B-E). Hence, CAF-derived THY1 endows HUVECs with additional cell-cell adhesion properties.

We explored whether CAF-derived THY1 is also involved in leukocyte recruitment in breast cancer. 4T1 cells and pCAFs expressing shCtrl or shTHY1 (fig. S2F) were orthotopically injected in the

mammary fat pad of BALB/c mice and, after 2 weeks, we used immunohistochemical staining to determine the presence and the location of the $CD11b^+$ immune infiltrate. We focused on $CD11b^+$ cells within and proximate to tumor blood vessels (Fig. 3H-L), to exclude resident $CD11b^+$ populations such as macrophages or dendritic cells. We found that the amount of $CD11b^+$ staining within the tissue in close proximity to veins was higher in tumors containing shCtrl pCAFs compared with those containing shTHY1 pCAFs (Fig. 3H). In contrast, tumors containing shCtrl pCAFs showed a lower amount of $CD11b^+$ staining within the blood vessels compared with tumors containing shTHY1 pCAFs (Fig. 3I), suggesting that leukocytes are less able to extravasate in tumors with shTHY1 pCAFs. The tumor weight was similar between the two conditions (fig. S2G); this result is in line with other studies showing that THY1 is a marker of tumor-promoting CAFs, rather than an effector of this phenotype [52, 53]. Overall, these results suggest that the transfer of THY1 from pCAFs to ECs can promote their interaction with $CD11b^+$ cells, thus influencing immune cell recruitment to tumor sites.

Different types of CAF-derived EVs contain the proteins transferred to ECs

Next, we investigated how pCAFs transfer their proteins to HUVECs. Our data showed that a high number of transferred proteins belonged to lipid bilayer-enclosed vesicles (Fig. 2C), supporting that EVs can be a major route of intercellular protein transfer. CM-EVs are involved in protein transfer [21, 22, 48, 54, 55], but the role of MBVs has not been investigated. We isolated EVs from both the CM and extracellular matrix of pCAFs (Fig. 4A). Electron microscopy analysis showed that the two EV types had a similar morphology (Fig. 4B). Nanoparticle tracking analysis showed that the diameter of both types of EVs ranged between 50 and 350 nm (Fig. 4C). However, the amount and size distribution differed between the two EV types. Those in the CM mainly included small particles with a diameter between 50 and 150 nm, whereas MBVs mostly consisted of large EVs, with major peaks at 150 nm and 200 nm (Fig. 4C-D and fig. S3A).

We molecularly characterized pCAF-derived EVs using MS proteomics (Data File S3). This analysis confirmed that both types of particles contain common EV markers, such as the tetraspanins CD63, CD81, and CD9 [30] and syntenin-1 (SDCBP) [56], but also highlighted differences, such as the relative abundance of some EV markers and the presence of ADP-ribosylation factor 6 (ARF6) and tumor susceptibility gene 101 protein (TSG101) only in MBVs and CM-EVs, respectively (Fig. 4E and Data File S3). Hence, our data have identified distinct traits of CM-EVs and MBVs.

We next compared the proteome of pCAF-derived EVs with the proteome of large-medium and small EVs of three publicly available datasets (fig. S3B-C) [57-59]. For each dataset, we selected proteins unique to each EV subpopulation and those with significantly different abundance between the two subpopulations. Then, we matched this subset to EV proteins whose abundance was significantly different between CM-EVs and MBVs (Data File S3). This analysis showed that proteins typically found in large-medium EVs were generally more abundant in MBVs. In contrast, proteins typically found in small EVs were more abundant in CM-EVs (fig. S3C). This observation was consistent across the three datasets (fig. S3C). Furthermore, proteins identified only in CM-EVs displayed enrichment for endosome-related GOCC terms (fig. S3D) and endosomes are one of the documented intracellular origins of small EVs (fig. S3B). Conversely, unique proteins in MBVs displayed enrichment in GOCC terms associated with plasma membrane, cytosol, ER and mitochondria (fig. S3D), which are expected in large-medium EVs because of their biogenesis [30].

The majority of pCAF proteins transferred to ECs during co-culture were identified in both EV types (Fig. 4F, Data File S1 and Data File S3), and their abundance positively correlated to the amount measured in the EVs (Fig. 4G, Data File S1 and Data File S3). Notably, the majority of the transferred plasma membrane receptors and membrane-bound ligands, including THY1, were more abundant overall in the MBVs (Fig. 4H and Data File S3). Overall, these results support that

each extracellular compartment contains different subsets of EVs, which carry the proteins transferred from CAFs to HUVECs.

MBVs have a major role in protein transfer to ECs

Next, we measured whether pCAF-derived CM-EVs and MBVs could transfer proteins to ECs. Because these EV types exist in different extracellular sites, we measured protein transfer when CAFs were co-cultured in physical contact (direct co-culture) or not (indirect co-culture) with HUVECs (Fig. 5A). In direct co-culture, HUVECs were exposed to both types of EVs, whereas in indirect co-culture to CM-EVs only (Fig. 5A). The amount of transferred proteins in direct co-cultures was more than two-fold higher compared to indirect co-culture (Fig. 5A, B). We used the same co-culture conditions to measure THY1 transfer from pCAFs to HUVECs. As for total proteins, the transfer of THY1 mainly occurred when cells were in direct culture (Fig. 5A, C). These results suggest that MBVs have increased protein transfer ability compared with CM-EVs. The matrix produced by CAFs influences many cell functions [35, 60], leading us to evaluate whether it could also sustain the ability of MBVs to act as vehicles for proteins. We compared the ability of EVs to transfer proteins when they were coated on pCAF-derived matrix compared to when they were coated on gelatin or on the matrix produced by patient-derived normal fibroblasts (pNFs) (fig. S4A), which has different composition and mechanical properties from pCAF-derived matrix [35]. We found that compared with CM-EVs, MBVs retained the ability to transfer more proteins, including THY1, when they were coated on gelatin or on fibroblast-derived matrix before HUVECs were plated on top (fig. S4A-C). The MBV-mediated transfer of THY1 to HUVECs was enhanced by the presence of the matrix compared with gelatin (fig. S4A, B). However, MBVs transferred the same amounts of proteins whether they were coated on the matrix produced by pNFs or pCAFs (fig. S4A, C); the same results were observed when the matrices were pre-treated with CM-EVs (fig. S4A, C). These data indicate that pNF- and pCAF-derived matrices have common features that

promote the EV-mediated protein transfer, but the matrix alone is not able to account for the different efficiency in protein transfer between CM-EVs and MBVs.

To confirm the different role of CM-EVs and MBVs in protein transfer, we also added them directly into the HUVEC culture medium. In line with the previous results, HUVECs received significantly more proteins when treated with MBVs than with CM-EVs, although the difference was less pronounced (Fig. 5A, D). MBVs still had a higher protein transfer ability compared with CM-EVs even when HUVECs were treated with equal numbers of the two EV types (fig. S4D-E). Moreover, upon treatment with MBVs, five-fold more HUVECs positively stained for THY1 compared with when treated with CM-EVs, and THY1 amount was two-fold higher (Fig. 5A, E).

To confirm that pCAF-derived THY1 transferred by MBVs mediates monocyte adhesion to HUVECS, HUVECs were treated with equal numbers of pCAF-derived CM-EVs or MBVs isolated from pCAFs either silenced or not for THY1 (Fig. 5A, F). Microscopy analysis showed that HUVECs treated with MBVs bound a higher number of monocytes compared with untreated HUVECs or HUVECs that were treated with CM-EVs (Fig. 5F). However, the MBV pro-adhesive effect was entirely lost when these EVs were isolated from THY1 silenced pCAFs (Fig. 5F). Together, our data provide evidence that MBVs are a major vehicle for protein transfer from mammary CAFs to HUVECs and that they can influence HUVEC function.

α-SMA^{high} TNFRSF12A^{high} CAFs are the major donors of proteins to ECs

Human normal fibroblasts (NFs) activated upon treatment with CM of prostate and melanoma cancer cells transfer more proteins compared with untreated fibroblasts [21]. Therefore, we compared protein transfer of our mammary CAFs with their matched NFs isolated from the same patient (pNFs), derived from macroscopically healthy tissue adjacent to the tumor. We found that pCAFs transferred more proteins to HUVECs than pNFs (Fig. 6A, B), and confirmed this result using microvascular endothelial cells (MVECs) (fig. S5A, B). Because we showed that EVs are involved in

protein transfer, we compared the amounts of EVs released by pCAFs and pNFs. Nanoparticle tracking analysis showed that pCAFs deposited significantly more medium-large EVs in the ECM than their NF counterpart (Fig. 4A, C-D and fig. S3A). In contrast, pNFs and pCAFs released EVs of similar size and quantity into the CM (Fig. 4C-D and fig. S3A). Notably, HUVECs treated with CAF-derived MBVs received more proteins than when treated with MBVs produced by pNFs (Fig. 6A, C). Moreover, CM-EVs and MBVs secreted by pNFs transferred a comparable amount of proteins to HUVECs (Fig. 6A, D). However, the different protein transfer ability between pNF- and pCAF-derived MBVs was greatly reduced when HUVECs were treated with equal numbers of MBVs (fig. S4D-E). Together, these results suggest that CAFs transfer more proteins because they produce more MBVs. Despite this, MBVs isolated from pCAFs and pNFs were molecularly and functionally different. In fact, significantly more monocytes adhered to HUVECs treated with MBVs isolated from pCAFs compared with pNFs, even though equal numbers of EVs were used (Fig. 5F).

Our pCAF lines transferred different amounts of proteins to ECs (fig. S5A, C) raising the question of whether all CAFs can transfer proteins. To address this question, we first measured the correlation between the abundance of common CAF markers in our pCAF lines (Data File S4), including ACTA2, prolyl endopeptidase FAP (FAP), integrin beta-1 (ITGB1), dipeptidyl peptidase 4 (DPP4), platelet-derived growth factor receptor alpha and beta (PDGFRA and PDGFRB), caveolin-1 (CAV1) and protein S100-A4 (S100A4, also known as FSP-1), with their protein transfer ability. We found that the amount of proteins transferred by fibroblasts significantly correlated only with ACTA2 protein abundance (Fig. 6E). Microscopy analysis for α-SMA in our pCAF lines confirmed the proteomic data showing that the pCAF1 line, which transferred the most proteins to ECs (fig. S5A, C), contained more cells with high α-SMA protein amount than pCAF3 and pCAF4 lines (Fig. 7A-B). Similarly, western blot analysis showed that α-SMA protein amount was higher in pCAF1 line compared with pCAF3 and pCAF4 lines (Fig. 7C). To assess whether pCAFs expressing high or

low protein amount of α-SMA had different protein transfer abilities, we needed to identify cell surface proteins to sort the two living subpopulations for functional assays. To achieve this, we analyzed CAFs sorted according to high and low α-SMA protein amount by MS proteomics (fig. S6A). Principal component analysis of 2,080 proteins quantified across the three pCAF lines separated the α-SMA^{low} and α-SMA^{high} subpopulations (fig. S6B and Data File S5). Moreover, 67 proteins showed difference in abundance between α-SMA^{low} and α-SMA^{high} subpopulations in at least two of the three pCAF lines (Fig. S6C and Data File S5) and among those, there were 7 cell surface receptors (Fig. 7D). We followed up on the tumor necrosis factor receptor superfamily member 12A (TNFRSF12A, also known as FN14, TweakR or CD266), because its abundance was highly different between α-SMA^{low} and α-SMA^{high} CAFs and it was a good candidate for cell sorting (Data File S5). Immunofluorescence staining for α-SMA confirmed that there were more α-SMA^{high} cells in TNFRSF12A^{high} sorted pCAFs than in TNFRSF12A^{low} pCAFs (fig. S6D). On average, TNFRSF12A^{high} pCAFs transferred double the amount of proteins to co-cultured HUVECs than TNFRSF12A^{low} pCAFs (Fig. 7E, F), including THY1 (Fig. 7E, G). Moreover, TNFRSF12A^{low} pCAFs had a protein transfer ability similar to that of their NF counterpart (Fig. 7E, F). Consistent with our findings that identified the MBVs as a major vehicle for protein transfer, HUVECs treated with TNFRSF12A^{high} pCAF-derived MBVs received more proteins than when treated with CM-EVs isolated from the same CAF subpopulation (Fig. 7H). Instead, the protein transfer ability of CM-EVs and MBVs isolated from TNFRSF12A^{low} pCAFs was similar and lower than the amount of proteins transferred by TNFRSF12A^{high} pCAF-derived MBVs (Fig. 7H). The different protein transfer ability between MBVs from TNFRSF12A^{high} and TNFRSF12A^{low} pCAFs did not depend on evident differences in the matrices produced by the two CAF subpopulations, as the amount of fibrillar collagen (CNA35) and fibronectin was similar between the two (Fig. 7I). Hence, α-SMA^{high}

mammary CAFs enriched using the transmembrane receptor TNFRSF12A have enhanced ability to transfer proteins to ECs.

α-SMA^{high} TNFRSF12A^{high} CAFs express high amounts of myofibroblast markers

α-SMA^{high} CAFs are typically those referred to as myCAFs, whereas α-SMA^{low} are typically iCAFs [15, 16]. Therefore, we investigated the expression of other myCAF and iCAF markers in our CAF subpopulations. We sorted TNFRSF12A^{high} and TNFRSF12A^{low} pCAFs, expanded them in culture, and assessed the expression of CAF markers by RT-qPCR. This analysis confirmed that TNFRSF12A^{high} pCAFs expressed higher amounts of *ACTA2* and other genes highly expressed in mammary myCAFs [7, 16, 61], such as those encoding collagen alpha-1 (I) chain (*COL1A1*) and transgelin (*TAGLN*), compared with TNFRSF12A^{low} pCAFs (fig. S7A-B). Conversely, we did not detect significant differences in mRNA amounts of stromal cell-derived factor 1 (*SDF1*, also known as C-X-C motif chemokine 12 or *CXCL12*) and interleukin-6 (*IL6*), which are highly expressed in mammary iCAFs [7, 16, 61] (fig. S7A-B). Similarly, decorin (*DCN*), which expression is analogous in all CAFs [7, 61], had similar mRNA amounts in our two sorted populations (fig. S7A-B). These data suggest that high amounts of the TNFRSF12A receptor are found in CAFs with the myCAF phenotype. Consistent with this observation, in two publicly available single-cell RNA sequencing datasets of CAFs isolated from patients with breast cancer [7, 16], we found that both *ACTA2* and *TNFRSF12A* mRNA amounts were high in the subpopulation defined by the authors as myCAFs (Fig. 8A-B). In addition, immunofluorescence staining of tumor tissue sections from patients with breast cancer confirmed the presence of TNFRSF12A^{+} and α-SMA^{+} CAFs in the stroma and showed that these cells could be found in close proximity to blood vessels (Fig. 8C and fig. S8). Hence, enhanced CAF-EC communication based on protein transfer is distinctive of those CAFs with a myofibroblast-like phenotype.

Discussion

Using CAFs isolated from patients with breast cancer, we have discovered that CAFs with a myofibroblastic-like phenotype transfer high amounts of proteins to the surrounding endothelium. The transfer of proteins mainly occurs through MBVs. Using THY1 as an example of transferred protein, our work also shows that transferred proteins can influence the phenotype of the endothelium (Fig. 8D). CAFs in different states secrete distinct subsets and amounts of soluble factors and ECM components, which determine their functions in the tumor [15]. Therefore, understanding the heterogeneity of CAFs by associating their states with specific biological functions is fundamental to designing drugs for cancer treatment.

CAFs use EVs [14] and intercellular transfer of proteins to affect the function of neighboring cells in vitro [21, 22]. Although these mechanisms have been originally described between CAFs and cancer cells, using various MS-based proteomic approaches we showed that ECs also receive proteins from CAFs in vitro. Moreover, we provide evidence that this process may occur in vivo. What is the fate of these proteins in recipient cells? It has been suggested that the fate of the EV cargo depends on the mechanism of EV internalization [62, 63]. For example, EV cargo can be directed toward lysosomes for degradation or can escape it [62-64]. Here, we showed that CAF-derived proteins could be functional in recipient cells: ECs can receive plasma membrane proteins from CAFs, most of which are involved in migration and cell-cell or cell-matrix adhesion. Among them, THY1 enhanced the ability of ECs to interact physically with THP-1 monocytes in vitro and supported the recruitment of $CD11b^+$ leukocytes in orthotopic 4T1 tumors. The ability of CAFs to affect the extravasation of $CD11b^+$ leukocytes has the potential to influence the composition of the immune microenvironment, whose variation plays a crucial role in determining the efficacy of the therapeutic strategies [65]. Proteins transferred by cancer cells or CAFs influence the phenotype of recipient cells [21, 22, 48, 54, 55]. For example, PC3 human prostate cancer cells

391 increase the migration of prostate cancer and benign prostatic hyperplasia cells through the
392 exosomal transfer of integrin αvβ3 [54]. Moreover, HeyA8 and TYK-nu human epithelial ovarian
393 cancer cells induce an invasive mesenchymal phenotype of human peritoneal mesothelial cells
394 through the transfer of exosomal CD44 [55] and activated human prostate and dermal fibroblasts
395 support migration of cancer cells by transferring galectin-1 through ectosomes [22]. We found
396 that CAFs transferred all these proteins to ECs and that CD44 and ITGB3 were among the receptors
397 with the highest exogenous fraction. This suggests that, in addition to THY1, CD44 and ITGB3 may
398 influence EC functions.
399 The ECM is an important source of signals that actively regulate tumor progression. Its structure
400 and composition, including ECM-associated proteins such as growth factors, influence many
401 aspects of tumor pathology [66-68]. It is now evident that EVs have an essential role in ECM
402 biology: EVs can be functional components of the ECM [32, 34] and CM-EVs control ECM
403 deposition [69] and remodeling [70]. Our work provides evidence that CAFs deposit EVs in the
404 matrix and that MBVs play a key role as vehicles for intercellular protein transfer. MBVs and CM-
405 EVs contain EVs of different sizes, and our MS proteomic characterization identified several
406 differences between these two EV types, in accordance with previous work [33]. In particular, our
407 findings support the concept that CM-EVs and MBVs may have different intracellular origins,
408 specifically endosomal for CM-EVs and plasma membrane for MBVs, and provides evidence that
409 these two subsets of vesicles have distinct functions. In fact, MBVs can deliver a greater amount
410 of proteins to ECs and promote the adhesion of monocytes to ECs compared with CM-EVs. We
411 showed that the ability of MBVs to deliver more proteins to recipient cells was due to their distinct
412 characteristics rather than their extracellular location. This specific function of MBVs could
413 depend on their larger size enabling them to transport a higher amount of proteins or on the
414 presence of surface receptors that make their uptake easier compared with CM-EVs. Our data also

suggest that CM-EVs and MBVs are heterogeneous populations that may interact differently with recipient cells. EVs can influence recipient cell function through ligand-receptor interactions without being internalized [63, 71], and EV cargo can also be re-released in the extracellular space [72]. The existence of multiple ways of interaction between EVs and recipient cells is also indicated by our proteomic analysis, which identifies EV proteins that are not transferred to ECs, although we cannot exclude that some transferred proteins are below levels detectable by MS or degraded in lysosomes [63] Further study will be required to elucidate the precise mechanism by which MBVs can transfer more protein.

We showed that CAFs secreted more MBVs than their normal-like fibroblast counterpart. This explains why CAFs have a greater capacity to transfer proteins to the endothelium. Based on this, we argue that protein transfer from fibroblasts is a phenomenon predominant in pathological conditions. Our work also indicates that CAF-derived MBVs may play unique roles in altering tumors locally, in addition to being a source of systemic signals, which is a classical function associated with tumor-derived EVs [73].

MyCAFs deposit most of the tumor ECM and contribute to its remodeling [16, 68]. Our work indicates that there are additional ways through which myCAFs can influence cellular functions. We showed that myCAFs were the major donors of proteins to ECs and that myCAF-derived MBVs had a key role in the process of protein transfer. However, we found no evidence that the matrix produced by myCAFs supported MBV performance, further confirming that MBVs transferred more proteins because of other distinct properties. These findings suggest that the increased protein transfer from myCAFs to ECs could depend on their ability to deposit different types and/or amounts of MBVs in the matrix. Another interesting aspect that emerged from our work is that MBVs could be a source of nutrients for tumor and stromal cells. Cancer cells [20, 74, 75] and ECs [76] take up proteins and amino acids from the extracellular milieu and use them for

macromolecule synthesis, and to modulate redox homeostasis [77]. In recipient cells, CAF-derived proteins may undergo proteolytic degradation and supply amino acids that contribute to biosynthetic and bioenergetics processes. Hence, we would speculate that MBVs could be an additional mechanism for local exchange of nutrients within the TME [78].

Finally, we have identified TNFRSF12A as potential cell surface marker of mammary CAFs with myofibroblast-like phenotype to be added to the small panel of plasma membrane proteins that can be used to isolate these cells for functional characterization [15]. Indeed, after the exclusion of epithelial cells, immune cells, ECs and pericytes, TNFRSF12A allows the direct selection of CAFs expressing high levels of myofibroblast markers. This result is in line with another study showing that TNFRSF12A specifically belongs to the myCAF transcriptional profile [16].

In conclusion, our work has identified that myCAFs can transfer functional proteins to ECs through MBVs. Our work paves the way for studies seeking to explore whether and how other transferred plasma membrane proteins can modify endothelial cell phenotype and how this affects the function of the tumor vasculature and influences tumor development and progression in vivo. These results will inform on whether targeting the production of MBVs should be further investigated as a strategy to oppose cancer. As an example, the targeting of MBV production could impair THY1 transfer therefore affecting the composition of the immune microenvironment and the response to therapy. More work should also be done to understand MBV biogenesis and function, a mechanism that so far has been largely overlooked.

A limitation of our study is that we used mice that express RFP under the control of the *Acta2* promoter to test the transfer of proteins in vivo, and we cannot exclude that *Acta2*-expressing cells other than CAFs, such as pericytes surrounding the endothelium, also transfer proteins to ECs [79, 80]. However, CAFs expand during tumor progression and we showed that the amount of transferred proteins to ECs increased proportionally with CAF number in vitro. Hence, we think

that the majority of RFP found in the tumor endothelium could derive from CAFs. Another limitation is that we cannot exclude that CAFs had transferred *RFP* mRNA, which has then been translated into protein in the endothelium. Hence, additional studies are needed to further prove that CAFs transfer proteins to the endothelium in vivo, for example using MetRS* mice [81].

Materials and Methods

Cell culture

pCAFs and pNFs were isolated at the CRUK Scotland Institute from women with breast cancer and immortalized as previously described [35]. Samples were obtained through NHS Greater Glasgow and Clyde Bio-repository. Patients agreed with the use of their tissue samples for research. Unless otherwise stated, pCAFs and pNFs used for the experiments are pCAF1 and pNF1. cCAFs and cNFs were kindly provided by Professor Akira Orimo (Juntendo University, Tokyo) [35, 82]. Human MDA-MB-231 and mouse 4T1 breast cancer cells were purchased from ATCC. Luciferase-expressing 4T1 cells were kindly provided by Professor Gareth Inman (University of Glasgow and CRUK Scotland Institute, Glasgow). CAFs, NFs, MDA-MB-231 cells and 4T1 cells were cultured in Dulbecco's modified Eagle's medium (DMEM) supplemented with 10% fetal bovine serum (FBS), 2 mM glutamine and 1% penicillin/streptomycin (Life Technologies, Thermo Fisher Scientific). pCAFs and pNFs were cultured on dishes coated with collagen I from rat tail (12 µg/ml, Gibco, Thermo Fisher Scientific). HUVECs were isolated from donors using previously described methods [67]. HMVECs (100-05a) were purchased from Sigma-Aldrich. HUVECs and HMVECs were cultured on 1% gelatin coated dishes in EGM-2 or EGM-2 MV (Lonza), respectively.

THP-1 cells were purchased from ATCC and cultured in RPMI-1640 medium (Life Technologies) supplemented with 10% FBS, 2 mM glutamine and 0.05 mM 2-mercaptoethanol (Sigma-Aldrich). MCF10DCIS.com cells were kindly provided by Professor Philippe Chavrier (Institute Curie, Paris).

MCF10DCIS.com cells were cultured in F12 medium supplemented with 5% horse serum (Life Technologies), 2 mM glutamine and 1% penicillin/streptomycin. Jurkat cells were kindly provided by Dr. Shehab Ismail (University of Glasgow and CRUK Scotland Institute, Glasgow). Jurkat cells were cultured in RPMI-1640 medium supplemented with 10% FBS and 2 mM glutamine. For SILAC experiments, fibroblasts were cultured in SILAC DMEM (Life Technologies) supplemented with 2% FBS, 8% 10 kDa dialyzed FBS, 2 mM glutamine, 1% penicillin/streptomycin, 84 mg/l $^{13}C_6{}^{15}N_4$ L-arginine and 175 mg/l $^{13}C_6{}^{15}N_2$ L-lysine (Cambridge Isotope Laboratories, Inc.). All the cell lines were cultured under standard conditions (37°C and 5% CO_2) and were routinely tested for mycoplasma.

EV isolation

pCAFs or pNFs were plated in serum-free DMEM. After 48h, EVs were collected from both the CM and the matrix. The CM was collected, then the culture plate was washed with PBS and the EVs from the matrix were detached using Accutase® (Sigma-Aldrich) and collected in DMEM supplemented with 0.5% FBS, which had been previously ultracentrifuged at 100,000 x g for 5h and filtered with a 0.2 µm filter to reduce the amount of serum EVs. Cells and debris were removed by centrifugation at 300 x g (4°C, 10min) and 2,000 x g (4°C, 30min), and CM-EVs and MBVs were isolated by ultracentrifugation at 100,000 x g (4°C, 90min). Pelleted EVs were resuspended in PBS and subjected to another step of ultracentrifugation at 100,000 x g (4°C, 90min). EVs were collected in PBS and gently sonicated at 5 microns amplitude using a metal tip (Soniprep 150, MSE) three times for 5s before using them for protein transfer experiments and nanoparticle tracking analysis and before sample preparation for electron microscopy.

Small interfering RNA

Transient knockdown was performed using the Amaxa kit R (Lonza) and Nucleofector device (program T-20, Lonza) according to the manufacturer's protocol. $2x10^6$ CAFs were transfected

with 3 nM of non-targeting control (siCtrl, D-001810-10-05, GE Healthcare Dharmacon, Inc.) or THY1 human siRNA (siTHY1, L-015337-00-0005, GE Healthcare Dharmacon, Inc.). CAFs were used for experiments 72h after transfection.

Nanoparticle Tracking Analysis

CM-EVs and MBVs were isolated as described above from $1.5x10^5$ pCAFs or pNFs, which were seeded in serum-free medium in 6 cm cell culture dishes. After isolation, the EVs were resuspended in 1 ml of PBS. EV size and concentration were determined using a NanoSight LM10 (Malvern Panalytical) and the NTA 3.1 software. Each measurement is the result of three acquisitions of 60s. The camera level was set to 14 and the detection threshold to 4. The PBS used for EV isolation and collection was filtered with the 0.02 µm filter.

Intercellular protein and THY1 transfer

To measure the intercellular protein transfer in co-culture, donor cells were labeled with 10 µM CellTrace™ CFSE (Life Technologies) in PBS for 20min at 37°C. After at least 1h, donor cells were seeded. Once they were adhered, recipient cells were seeded in co-culture with donor cells for 24h (also referred to as direct co-culture). For indirect co-culture, donor cells were plated on glass coverslip, which was positioned upside down on the culture dish where recipient cells were seeded. The glass coverslip was placed above a polytetrafluoroethylene film (PTFE) ring with a thickness of 0.08 mm (Goodfellow Cambridge Ltd). After 24h of co-culture, cells were detached with Accutase®, resuspended in FACS buffer (25 mM HEPES, 5 mM EDTA, 1% penicillin/streptomycin, 1% FBS in PBS) and the transfer of CFSE labeled proteins was analyzed by an Attune™ NxT flow cytometer (Thermo Fisher Scientific) and FlowJo software version 10.7.1. To measure THY1 transfer, cells were detached with Accutase® after 24h of co-culture, resuspended in FACS buffer, incubated with APC anti-THY1 antibody (1/100, [5E10] 328114 BioLegend, RRID:AB_893431) and human TruStain FcX™ (1/200, BioLegend) for 45min on ice (100 µl/10^6

cells). DAPI (Sigma-Aldrich) was used as a live/dead marker. THY1 transfer was analyzed by an Attune^{TM} NxT flow cytometer and FlowJo software version 10.7.1. In both protein and THY1 transfer experiments, donor cells were gated as CFSE^{high} and recipient cells were gated as CFSE^{low}. Unless otherwise stated, donor cells and recipient cells were plated at 2:1 ratio. The medium used for the co-culture experiments was EGM-2 or EGM-2 MV depending on the EC type.

To measure the EV-mediated transfer of proteins, CM-EVs and MBVs were isolated from 1.5x10^5 pCAFs, pNFs or sorted pCAFs and labeled with 10 µM CellTrace^{TM} CFSE in PBS for 20min at 37°C. After labeling, EVs were washed in PBS by two sequential steps of ultracentrifugation at 100,000 x g (4°C, 90min). The whole amount of isolated EVs was used to treat 3x10^4 HUVECs in EGM-2. After 20h, HUVECs were detached and intercellular protein transfer was analyzed as above. In experiments in which recipient cells were treated with equal numbers of isolated CM-EVs or MBVs, vesicles were quantified by nanoparticle tracking analysis and used for the treatment. To measure the EV-mediated transfer of THY1, CM-EVs and MBVs were isolated from 5x10^4 pCAFs and the whole amount was used to treat 2.5x10^4 HUVECs in EGM-2. After 3h, HUVECs were detached, stained for THY1 and analyzed as above. If not otherwise stated, all the protein and THY1 transfer experiments were performed on 1% gelatin coated dishes.

To determine whether the ECM influences the transfer of proteins and THY1, decellularized ECM was prepared by seeding pNFs or pCAFs at 100% confluence on 0.2% gelatin, which was crosslinked using 1% glutaraldehyde for 7 days. ECM was decellularized with 20 mM NH_4OH, 0.5% Triton X-100 (TX-100, Sigma-Aldrich) in PBS. CM-EVs and MBVs were isolated from 1.5x10^5 pCAFs and labeled as described above. After isolation, EVs were coated overnight on the decellularized ECM or on dishes previously coated with 1% gelatin. Unbound EVs were removed by washing with PBS and 3x10^4 HUVECs were seeded on top in EGM-2. After 20h, HUVECs were detached and intercellular protein and THY1 transfer were analyzed as above.

In protein and THY1 transfer experiments, recipient cells that were seeded without donor cells (also referred to as monoculture condition) or that were untreated with EVs were used as control to determine the levels of auto-fluorescence. In addition, in THY1 transfer experiments, recipient cells seeded in monoculture were stained for THY1 to determine basal amounts.

Western blotting analysis

Cells were lysed in 2% SDS in 100 mM Tris-HCl pH 7.4, incubated at 95°C for 5min, sonicated using a metal tip and centrifuged at 16,000 x g for 10min. Protein concentration was determined using Optiblot Bradford reagent (Abcam). Protein lysate was mixed with NuPAGE™ LDS sample Buffer 4x (Life Technologies) supplemented with 400 mM dithiothreitol (DTT, Sigma-Aldrich). Proteins (15-20 µg) were separated using 4-12% gradient NuPAGE™ Novex Bis-Tris gel (Life Technologies). Protein transfer was performed on methanol-activated Immobilon®-FL PVDF membrane (Sigma-Aldrich). Membranes were blocked for 1h in 5% bovine serum albumin (BSA, Sigma-Aldrich) in Tris-buffered saline with 0.1% Tween® 20 detergent (TBST) at room temperature and incubated with primary antibody overnight at 4°C. The following primary antibodies were used: THY1 (1/2,000, [D3V8A] 13801 Cell Signaling Technology), α-SMA (1/10,000, A5228 Sigma-Aldrich), GAPDH (1/1,000, sc-48167 Santa Cruz Biotechnology), vinculin (1/2,000, V9131, Sigma-Aldrich) and β-tubulin (1/1,000, sc-9104 Santa Cruz Biotechnology). Membranes were incubated with HRP-conjugated (1/2,500 New England Biolabs) or IRDye® (1/10,000 LI-COR Biosciences) antibody for 45min at room temperature. Western blot images were acquired using a myECL Imager (Thermo Fisher Scientific) or a LI-COR Odyssey CLx scanner (Image Studio software, version 5.0.21).

Immunofluorescence

For vimentin and fibronectin staining, cultured pCAFs and pNFs were fixed in 4% paraformaldehyde (PFA, Sigma-Aldrich), permeabilized and blocked with 0.1% TX-100 in 1% BSA in PBS for 30min, incubated overnight at 4°C with the following primary antibodies: vimentin

(1/50, sc-7557 Santa Cruz Biotechnology) and fibronectin (1/100, 610078 BD Biosciences, RRID:AB_397486). Cells were incubated with Alexa Fluor® 488 secondary antibody (1/400, Life Technologies) for 2h. DAPI (1/5,000) was used for nuclear staining. Images were acquired using a Zeiss LSM 710 confocal microscope (Carl Zeiss, EC Plan-Neofluar 20x/0.50 M27 objective, no immersion).

To evaluate protein transfer by immunofluorescence, pCAFs were labeled with CellTrace™ CFSE as described above and seeded on glass coverslips in a 24-well plate. Once they adhered, ECs were seeded in co-culture with pCAFs. After 24h, cells were fixed in 4% PFA. DAPI and Alexa® 647 Phalloidin (1/100, Life Technologies) were used for nuclear and F-actin staining, respectively. HUVECs seeded in monoculture condition were used as control. Images were acquired with a Zeiss LSM 880 confocal microscope in Airyscan mode (Carl Zeiss, Plan-Apochromat 63x/1.4 Oil DIC M27 objective, zoom 1.8, z-stacks of 5-9 µm, 28-48 slices). Images were Airyscan processed with Zen software (version 3.7) using default settings. The 3D reconstruction and analysis were performed using Imaris software (version 9.5, Bitplane, Oxford Instruments).

For α-SMA staining, $5x10^3$ pCAFs were seeded in each well of a 96-well plate. The following day, cells were fixed in 50% acetone/50% ethanol for 20min and permeabilized and blocked with 0.05% saponin (Sigma-Aldrich) in 1% BSA in PBS for 30min. Cells were incubated with anti-α-SMA antibody (1/200, [1A4] ab7817 Abcam) in 1% BSA in PBS for 1.5h and then with Alexa Fluor® 647 secondary antibody (1/250, Life Technologies) for 1h. HCS CellMask™ Green Stain (1/10,000, Life Technologies) and DAPI were used for cytoplasm and nuclear staining, respectively. For each well, 45 images were acquired on an Opera Phenix high-content imaging system (20x objective, z-stacks of 0.8 µm, PerkinElmer). Image analysis was performed using Harmony imaging analysis software (PerkinElmer, version 4.9).

pCAF sorting

Cultured pCAFs were detached with Accumax™ solution (Sigma-Aldrich) and resuspended in FACS buffer. To sort pCAFs based on α-SMA protein abundance, pCAFs were fixed and permeabilized by using the eBioscience™ Intracellular Fixation & Permeabilization Buffer Set (Life Technologies) according to the manufacturer's instructions. Cells were resuspended in permeabilization buffer (100 µl/10^6 cells) and incubated with anti-α-SMA antibody (1/1,000, [1A4] ab7817 Abcam) for 1h and then with Alexa Fluor® 488 or 647 secondary antibody (1/250, Life Technologies) supplemented with 2% donkey serum for 1h. Unstained pCAFs and pCAFs incubated with the secondary antibody only were used as controls. To sort pCAFs based on TNFRSF12A protein abundance, 10^6 cells were incubated with BD Horizon BV421 anti-TNFRSF12A antibody (1/140, 565712 BD Biosciences, RRID:AB_2739337) and human TruStain FcX™ (1/200, BioLegend) in 100 µl of FACS buffer for 45min on ice. Unstained pCAFs were used as control. pCAFs were sorted into α-SMA^{high} and α-SMA^{low} or TNFRSF12A^{high} (10% of cells with the highest expression) and TNFRSF12A^{low} (10% of cells with the lowest expression) using a BD FACSAria™ (BD Biosciences).

Collagen quantification in sorted pCAFs

TNFRSF12A^{high} and TNFRSF12A^{low} pCAFs were plated at confluence for 7 days. They were incubated with 1 µM of the fluorescent collagen binding CNA35-mCherry [83] for 1h, fixed in 4% PFA and counterstained with DAPI (1/5,000). Images were taken on a Zeiss LSM 710 confocal microscope and collagen staining was quantified using ImageJ software.

Adhesion Assay

To measure the binding of THP-1 cells to HUVECs that were directly co-cultured with pCAFs, control and THY1-silenced pCAFs were labeled with 2.5 µM CellTracker™ Green CMFDA Dye (Life Technologies) in PBS for 25min at 37°C and 2x10^4 labeled pCAFs were seeded in each 1% gelatin coated well of a 96-well plate. HUVECs were labeled with 1 µM CellTracker™ Deep Red Dye (Life Technologies) in PBS for 20min at 37°C and 4x10^4 labeled cells were seeded in co-culture with

pCAFs. After 24h of co-culture, $8.5x10^3$ THP-1 cells, which were labeled with 2 µM CellTracker™ Orange CMTMR Dye (Life Technologies) in PBS for 20min at 37°C, were added to each well in M199 medium (Life Technologies) supplemented with 10% FBS. After 45min, unbound THP-1 cells were removed by three washes in 1% BSA in PBS with calcium and magnesium (Sigma-Aldrich). Cells were fixed in 4% PFA and DAPI was used for nuclear staining.

To measure the binding of THP-1 cells to HUVECs that were treated with EVs, $1.5x10^5$ control pCAFs, THY1-silenced pCAFs and pNFs were seeded in serum-free medium in 6 cm cell culture dishes and EVs were isolated as described above. CM-EVs and MBVs were isolated from control and THY1-silenced pCAFs, MBVs only were isolated from pNFs. $4x10^4$ HUVECs were seeded in a 1% gelatin coated well of a 96-well plate and treated overnight with $5x10^8$ of isolated EVs. Unbound EVs were removed by washing the well with PBS with calcium and magnesium and $8.5x10^3$ THP-1 cells were added as described above. For each well, 25-45 images (adhesion assay in co-culture conditions) or 77 images (adhesion assay after EV treatment) were acquired on an Opera Phenix high-content imaging system (objective 20x and z-stacks of 2 µm for the adhesion assay in co-culture conditions, and objective 10x for the adhesion assay after EV treatment, PerkinElmer). Image analysis was performed using Harmony imaging analysis software (PerkinElmer, version 4.9). For each well, the number of THP-1 monocytes that bound HUVECs was averaged (adhesion assay in co-culture condition) or summed (adhesion assay after EV treatment). In the adhesion assay in co-culture conditions, only THP-1 cells overlapping the ECs at least for the 30% of their cellular body were counted.

NF/CAF characterization

pNFs, pCAFs, MCF10DCIS.com cells and HUVECs were detached with the Accumax™ solution and resuspended in FACS buffer. Jurkat cells were centrifuged and resuspended in the FACS buffer. 10^6 cells were incubated with the following antibodies (1/100, BioLegend): CD31-PE ([WM59]

303105, RRID:AB_314331), CD45-PE ([2D1] 368510, RRID:AB_2566370) and EPCAM-PE ([9C4] 324206, RRID:AB_756080), and with human TruStain FcX™ (1/200, BioLegend) in 100 µl of FACS buffer for 45min on ice. DAPI was used as a live/dead marker. An unstained sample composed of a mixture of all the above cells has been used as control. Cells were analyzed using a BD LSRFortessa™ Cell Analyzer (BD Biosciences) and FlowJo software version 10.7.1.

MS proteomic analysis

For trans-SILAC experiments, heavy-labeled pCAFs were labeled with CellTracker™ Green CMFDA Dye as described above and $1.5x10^6$ pCAFs were seeded in a gelatin coated 15 cm dish. After 16h, $7.5x10^5$ HUVECs were seeded in co-culture with pCAFs. HUVECs seeded without pCAFs (also referred to as monoculture condition) were used as control. After 4h and 24h, cells were detached with Accutase®, resuspended in FACS buffer and HUVECs were sorted as "CellTracker™ Green CMFDA Dye" negative cells by using a BD FACSAria™. Sorted HUVECs were lysed in 6 M urea/2 M thiourea supplemented with 10 mM tris(2-carboxyethyl)phosphine (TCEP) and 40 mM chloroacetamide (CAA) in 75 mM NaCl and 50 mM Tris-HCl (Sigma-Aldrich) and sonicated using a metal tip. 25-120 µg of proteins were digested with trypsin and were fractionated using high pH reverse phase fractionation. Briefly, dried peptides were resuspended in 200 mM ammonium formate adjusted to pH 10 with ammonium hydroxide solution (Sigma-Aldrich). Then, peptides were loaded on pipette-tip columns of ReproSil-Pur 120 C18-AQ 5 µm (Dr. Maisch HPLC GmbH), eluted in 7 fractions using an increasing amount of acetonitrile and analyzed by MS.

For the proteomic analysis of THP-1, α-SMA^{high} and α-SMA^{low} pCAFs, cells were washed three times in PBS and lysed in 6 M urea/2 M thiourea supplemented with 10 mM TCEP and 40 mM CAA in 75 mM NaCl and 50 mM Tris-HCl and sonicated using a metal tip. 10 µg of proteins were digested with trypsin, desalted using C18 StageTip [84] and analyzed by MS.

For the analysis of the pCAF1 proteome, cultured pCAFs were washed three times with PBS and cultured in serum-free DMEM. After 24h, cells were washed with PBS, lysed in 2% SDS with 1 mM DTT in 100 mM Tris-HCl pH 7.4, incubated at 95°C for 5min and sonicated using a metal tip. Tryptic peptides were generated from 150 µg of proteins using filter-aided sample preparation using filtration units with MW cutoff of 30 kDa [85, 86]. Briefly, lysates were loaded on the filter units, incubated for 20min with 55 mM iodoacetamide (IAA, Sigma-Aldrich) in 50 mM ammonium bicarbonate pH 8.0, digested with trypsin and eluted with 50 mM ammonium bicarbonate pH 8.0 (Sigma-Aldrich). 60 µg of peptides were fractionated using high pH reverse phase fractionation as described above and analyzed by MS.

For the analysis of the EV proteome, pCAFs were cultured in DMEM supplemented with 10% ultracentrifuged FBS. pCAFs were washed three times in PBS and cultured in serum-free DMEM. After 48h, CM-EVs and MBVs were collected as described above from $2x10^7$ and 10^7 pCAFs, respectively. After ultracentrifugation, EVs were collected in 200 mM HEPES pH 8.0 and 2,2,2-trifluoroethanol (TFE) was added 1:1 (Sigma-Aldrich). EVs were sonicated three times at 10 microns amplitude for 10s (with 20s on ice in between each sonication) and were incubated at 60°C for 1h at 1,000 rpm and sonicated again. EV lysates were incubated with 10 mM TCEP and 40 mM CAA for 1h. TFE concentration was reduced to 10% by adding 200 mM HEPES and EV lysates were digested with trypsin. Peptides were desalted using C18 StageTip, dried, resuspended in 200 mM HEPES and incubated with 0.1 mg Tandem Mass Tag (TMTzero™, Thermo Fisher Scientific) label reagent for 2h at 26°C and 450 rpm. Samples were dried, resuspended in 0.1% formic acid, acidified by adding trifluoroacetic acid (TFA, Sigma-Aldrich), desalted using C18 StageTip and analyzed by MS.

For the proteomic analysis of pCAFs and pNFs, cultured cells were washed with PBS, lysed in 2% SDS in 100 mM Tris-HCl pH 7.4, incubated at 95°C for 5min, sonicated using a metal tip and

centrifuged at 16,000 x g for 10min. Lysates were mixed 1:1 with an internal standard composed of a mix of SILAC heavy-labeled cCAFs/cNFs. Protein lysates were mixed with NuPAGE™ LDS sample Buffer (4x) and 1 mM DTT. Proteins were separated using 4-12% gradient NuPAGE™ Novex Bis-Tris gel, which then stained with Coomassie Blue. Gel lanes were cut into slices; proteins were in gel digested with trypsin [87]; and peptides were desalted using C18 StageTip and analyzed by MS.

MS analysis with a Q Exactive HF (trans-SILAC experiment and pCAF1 proteome)

Each of the 7 fractions was dried down and re-suspended in 2% acetonitrile/0.1% TFA in water and separated by nanoscale C18 reverse-phase liquid chromatography performed on an EASY-nLC II 1200 coupled to a Q Exactive HF mass spectrometer (Thermo Fisher Scientific). Elution was carried out for a total run time duration of 65min (fraction 1), 105min (from fraction 2 to 5) and 135min (fraction 6 and 7), using an optimized gradient. Peptides were eluted into a 50 cm (trans-SILAC) or 20 cm (pCAF1 proteome) fused silica emitter (New Objective, Inc., Littleton, MA) packed in-house with ReproSil-Pur C18-AQ, 1.9µm resin (Dr. Maisch HPLC GmbH). The emitter was kept at 50°C (trans-SILAC) or 35°C (pCAF1 proteome) by means of a column oven integrated into the nanoelectrospray ion source (Sonation). Eluting peptides were electrosprayed into the mass spectrometer using a nanoelectrospray ion source (Thermo Fisher Scientific). An active background ion reduction device (ABIRD, ESI source solutions) was used to decrease air contaminants signal level. Xcalibur software (Thermo Fisher Scientific) was used for data acquisition. Full scans over mass range of 375–1500 m/z were acquired at 60,000 resolution at 200 m/z. Multiply charged ions from two to five were selected through a 1.4 m/z window and fragmented. Higher energy collisional dissociation fragmentation was performed on the 15 most intense ions, using normalized collision energy of 27, and the resulting fragments were analyzed

in the Orbitrap at 15,000 resolution, using a maximum injection time of 25ms or a target value of 10^5 ions. Former target ions selected for MS/MS were dynamically excluded for 20s.

MS analysis with an Orbitrap Fusion™ Lumos™ (THP-1 cells, sorted pCAF and EV proteomes)

Desalted peptides were separated by nanoscale C18 reverse-phase liquid chromatography performed on an EASY-nLC 1200 coupled to an Orbitrap Fusion™ Lumos™ mass spectrometer (Thermo Fisher Scientific). Elution was carried out for a total run time duration of 265min (THP-1 and sorted pCAF proteome) or 135min (EV proteome), using a binary gradient with buffer A (water) and B (80% acetonitrile), both containing 0.1% of formic acid. Peptide mixtures were separated at 300 nl/min flow, using a 50 cm fused silica emitter (New Objective, Inc.) packed in-house with ReproSil-Pur C18-AQ, 1.9µm resin (Dr Maisch GmbH). The packed emitter was kept at 50°C by means of a column oven integrated into the nanoelectrospray ion source (Sonation). The eluting peptide solutions were electrosprayed into the mass spectrometer via a nanoelectrospray ion source (Sonation). An ABIRD (ESI source solutions) was used to decrease ambient contaminant signal level. Samples were acquired on an Orbitrap Fusion™ Lumos™ mass spectrometer. The mass spectrometer was operated in positive ion mode and used in data-dependent acquisition mode (DDA). Advanced Peak Determination was turned on and Monoisotopic Precursor Selection was set to “Peptide” mode. A full scan was acquired at a resolution of 120,000 (THP-1 and sorted pCAF proteome) or 60,000 (EV proteome) at 200 m/z, over mass range of 375-1500 m/z (THP-1 and sorted pCAF proteome) or 375-1400 m/z (EV proteome). The top 20 (THP-1 and sorted pCAF proteome) or 15 (EV proteome) most intense ions were selected using the quadrupole, fragmented in the ion routing multipole, and analyzed in the linear ion trap (THP-1 and sorted pCAF proteome) or analyzed in the Orbitrap at 15,000 resolution (EV proteome), using a maximum injection time of 35ms (THP-1 and sorted pCAF proteome) or 125ms (EV proteome), or a target value of $2x10^4$ ions (THP-1 and sorted pCAF proteome) or $1.5x10^5$ ions (EV proteome). Former

target ions selected for MS/MS were dynamically excluded for 60s (THP-1 and sorted pCAF proteome) or 30s (EV proteome).

MS analysis with an Orbitrap Elite (pNF and pCAF proteomes)

Digested peptides were separated by nanoscale C18 reverse-phase liquid chromatography performed on an EASY-nLC II (Thermo Scientific) coupled to a Linear Trap Quadrupole - Orbitrap Elite mass spectrometer (Thermo Fischer Scientific). Elution was carried out using a binary gradient with buffer A (water) and B (80% acetonitrile), both containing 0.1% of formic acid. Peptide mixtures were separated at 200 nl/min flow, using a 20 cm fused silica emitter (New Objective) packed in-house with ReproSil-Pur C18-AQ, 1.9µm resin (Dr Maisch GmbH) for a total duration of 255 minutes. Packed emitter was kept at 35°C by means of a column oven integrated into the nanoelectrospray ion source (Sonation). Eluting peptide solutions were automatically (online) electrosprayed into the mass spectrometer by a nanoelectrospray ion source (Sonation). An ABIRD was used to decrease ambient contaminant signal level. General mass spectrometric conditions of Linear Trap Quadrupole - Orbitrap Elite were as follows: spray voltage, 2.1 kV; ion transfer tube temperature, 200°C. The mass spectrometer was operated in positive ion mode and used in data-dependent acquisition mode (DDA). A full scan (FT-MS) was acquired at a target value of $1x10^6$ ions with resolution R = 120,000 over mass range of 300-1650 amu. The top ten most intense ions were selected for fragmentation in the linear ion trap using higher energy collision dissociation (HCD) using a maximum injection time of 150 ms or a target value of $4x10^4$ ions. Multiply charged ions from two to five charges having intensity greater than 40,000 counts were selected through a 3 amu window and fragmented using normalized collision energy of 30. Former target ions selected for MS/MS were dynamically excluded for 60s.

MS proteomic data analysis

The .RAW files were processed with MaxQuant software (version 1.5.5.1 for the proteome analysis of pCAF/pNF proteome, version 1.6.3.3 for all the other experiments) [88] and searched with the Andromeda search engine. The following setting was used: minimal peptide length 7 amino acids, trypsin specific digestion mode with maximum 2 missed cleavages, carbamidomethyl (C) as fixed modification, and oxidation (M) and acetylation (Protein N-term) as variable modifications. For the analysis of the EV proteome, TMTzero™ was added as fixed modification and maximum 4 missed cleavages were allowed. Minimum peptide ratio count was set to 2, except for the trans-SILAC experiment and the analysis of the pCAF1 proteome in which this parameter was set to 1. "Unique + razor" peptides were used for quantification in the analysis of the THP-1 and the pCAF and pNF proteomes; "unique" peptides were used for quantification in all the other experiments. The "match between runs" option was enabled for the analysis of pCAF/pNF proteome. For SILAC experiments, multiplicity was set to 2: light labels were Arg0 and Lys0; heavy labels were Arg10 and Lys8. Label free quantification (LFQ) setting was enabled for all the other experiments. The false discovery rates (FDRs) at protein and peptide levels were set to 1%.

Perseus software (version 1.5.5.3 for the analysis of pCAF/pNF proteome and version 1.6.2.2 for all the other experiments) [89] was used for data analysis. Potential contaminants, reverse peptides and proteins only identified by a modification site were filtered out. Only proteins identified with at least one unique peptide were kept for the analysis. To define the transferred proteins in the trans-SILAC experiment, we selected proteins with a "Ratio H/L count" value higher in HUVECs co-cultured with CAFs compared with monoculture. In addition, we selected proteins with an intensity value in the heavy channel (Intensity H) but not in the light one (Intensity L). The exogenous fraction was calculated as: 1-[1/(x+1)], where x is the "Ratio H/L" value. The exogenous fraction of proteins with an "Intensity H" value but not the "Intensity L" one was set to 1. The proteins with an exogenous fraction in at least three out of five biological replicates were selected.

We filtered out proteins not identified in the pCAF1 proteome (donor cells). For the analysis of the THP-1 proteome, the intensity value of each protein was divided by the molecular weight (MW) and transformed by $\log_2$. The adhesion molecules were selected based on the Gene Ontology Biological Processes (GOBP) category of cell adhesion (GO:0007155) and based on the subcellular location's annotations retrieved from UniProt. For the analysis of the pCAF1, CM-EV and MBV proteomes, the intensity value of each protein was divided by the MW and transformed by $\log_2$. For the analysis of the pCAF and pNF proteomes, the SILAC ratio was inverted, transformed by $\log_2$ and normalized by subtracting the median from each column. For the analysis of the α-SMA^{high} and α-SMA^{low} pCAF proteome, LFQ intensity was transformed by $\log_2$, three valid values were required for at least one pCAF1 or pCAF3 subpopulation and one valid value was required for at least one pCAF4 subpopulation. Missing values were replaced from the normal distribution using the recommended setting in Perseus software and proteins with a fold change ≥ 1.5 and $P \leq 0.05$ (two-tailed *t*-test) in at least two out of the three pCAF lines were selected. The Z-score was calculated by row. The cell surface proteins were selected based on the subcellular location's annotations retrieved from UniProt.

Proteomic datasets

EV proteomic data were downloaded from three publicly available datasets [57-59]. For each dataset, we considered the proteins unique to each EV subpopulation and those with an abundance significantly different between the two subpopulations as statistically analyzed by the authors, except for [59], we considered proteins with at least a two-fold change and $P < 0.05$. The selected proteins were matched by gene name with the proteins whose abundance was significantly different between CM-EVs and MBVs (two-tailed *t*-test, $P < 0.05$). The Z-score was calculated by row.

In vivo study of RFP transfer

BALB/c C.FVB-tg(Acta2-DsRed)1RK1/J mice (JAX stock #031159, generated by Dr. Raghu Kalluri, University of Texas MD Anderson Cancer Center, and kindly provided by Dr. Chris D Madsen, Lund University) were used for the in vivo experiments. All mouse procedures were in accordance with ethical approval from University of Glasgow under the revised Animal Act 1986 (Scientific Procedures) and the EU Directive 2010/63/EU authorized through UK Home Office Approval (Project license number 70/8645). For FACS analysis, $2.5x10^4$ 4T1 cells were resuspended in 100 µl of PBS and injected in the tail vein of 6-8-week-old RFP expressing female mice. Littermate α-SMA-RFP female mice that had not been injected with 4T1 cells were used as control. Mice were culled three weeks after the injection. Lungs were collected, minced finely and digested in pre-warmed PBS (with calcium and magnesium) with 2 mg/ml of collagenase A (Roche) for 1h on a rotating wheel at 37°C. The pieces of lung tissue were then passed through a 14G needle. Isolated cells were resuspended in M199 medium supplemented with 10% FBS, passed through a cell strainer (70 µm) and washed several times by centrifugation at 300 x g for 5min. Cells were resuspended in FACS buffer and incubated with the following antibodies (1/100, BioLegend): CD31-Alexa Fluor® 488 ([390] 102414, RRID:AB_493408) and CD45-APC/Cyanine7 ([30-F11] 103116, RRID:AB_312981) and with mouse TruStain FcX™ (1/200, BioLegend) for 45min on ice. DAPI was used as a live/dead marker. ECs were identified as $CD31^+CD45^-$ cells. Cells were analyzed using an Attune™ NxT flow cytometer and FlowJo software version 10.7.1.

For immunofluorescence analysis, $2.5x10^4$ 4T1 cells were resuspended in 100 µl of PBS and injected in the tail vein of 4-5-month-old female mice expressing or not (control mice) RFP. Mice were culled three weeks after the injection. A small incision was made in the trachea and 1 ml of 2% low-melting point agarose was introduced slowly into the lungs through a 22G needle. Lungs were excised and fixed in 4% PFA for 2h at 4°C. Then, lungs were sliced into 300 µm thick sections by using a vibrating microtome (Campden Instruments Ltd). Slices were permeabilized and

blocked for 5h in PBS with 1% BSA, 10% normal goat serum (NGS, Sigma-Aldrich), 0.3% TX-100, and 0.05% sodium azide (VWR International), incubated overnight with anti-CD31 antibody (1/200, [2H8] MA3105 Invitrogen, RRID:AB_223592) and then for 3h within Alexa Fluor® 647 secondary antibody (Jackson Immuno Research Labs) diluted in the same buffer. DAPI was used for nuclear staining. Slices were fixed in 4% PFA for 30min, incubated for 45min with Ce3D clearing solution and mounted with the Ce3D solution [90]. Images were acquired with a Zeiss LSM 880 confocal microscope in Airyscan mode (Carl Zeiss, Plan-Apochromat 63x/1.4 Oil DIC M27 objective, zoom 1.8, z-stacks of 10-14.5 µm, 41-58 slices). Images were Airyscan processed in Zen software (version 3.7) using default settings. Imaris software (version 9.5) was used to generate the 3D images and to calculate both the distance between RFP and CD31 surface, and the volume of RFP surface.

Haematoxylin & eosin staining of lungs

Haematoxylin & eosin (H&E) staining was performed on 4 µm formalin fixed paraffin embedded sections (FFPE) which had previously been heated at 60°C for 2h. H&E staining was performed on a Leica autostainer (ST5020). FFPE sections were dewaxed and taken through graded alcohols before being stained with Haem Z (RBA-4201-00A, CellPath) for 13min. Sections were washed in tap water, differentiated in 1% acid alcohol (3 dips), washed in tap water and the nuclei were blued in Scotts tap water substitute (made in-house). After washing the sections were placed in Putt's eosin (made in-house) for 3min. To complete H&E staining, sections were rinsed in tap water, dehydrated through graded ethanols and placed in xylene. The stained sections were coverslipped in xylene using DPX mountant (SEA-1300-00A, CellPath).

Orthotopic 4T1 mammary tumor experiments

pCAFs were transduced with a lentiviral vector encoding shCtrl (SHC016, Sigma-Aldrich) or shTHY1 (sc-42837, Santa Cruz Biotechnology). Cells were selected using 1.5 µg/ml puromycin. $0.25x10^5$

4T1 cells and 1.25x10^5 CAFs expressing either shCtrl or shTHY1 were mixed in a volume of 50 µl PBS and co-injected orthotopically into the fat pad of 8-week-old female BALB/c nude mice (Charles River). Mice were randomly allocated to the two groups. The tumors were harvested 14 days after inoculation. FFPE sections were stained for CD31 (1/75, ab28364 Abcam) on the Agilent autostainer using TRS high retrieval buffer (Agilent K8004) and for CD11b (1/5000, ab133357 Abcam) on the Leica Bond autostainer using Epitope retrieval buffer 2 (Leica AR9640) for 20min. Quantitative analysis was performed on serial FFPE mouse tumor sections using Halo software (version 3.1.1076.363, Indica Labs). Veins were selected based on the morphology and CD31 staining in the adjacent section. Software parameters were set which defined the stain of interest and all sections were analyzed using the same settings.

Electron Microscopy

CM-EVs and MBVs were isolated from pCAFs as described above, fixed in 4% PFA, ultracentrifuged at 100,000 x g (4°C, 90min) and resuspended in PBS. Drops of 5 µl of CM-EV and MBV suspensions were loaded onto carbon coated 400-mesh copper grids (Agar Scientific Ltd), which had been previously glow discharged (Quorum Q150T ES High Vacuum Unit settings 20 mA/30s). Samples were left to absorb onto carbon surfaces for 30min. Grids were floated on 100 µl droplets of PBS followed by fixation on a 50 µl droplet of 1% glutaraldehyde (Agar Scientific Ltd) for 5min. Grids were washed with distilled water before they were contrast stained with uranyl oxalate (Merck UK) pH 7.0 (10min in the dark) and embedded in methylcellulose/uranyl acetate (Merck UK) (10min on ice in the dark). Grids were scooped up on platinum loops and excess fluid gently drained off, leaving thin films. Grids were left to dry before they were picked off and stored in a grid box. Samples were viewed on a JEOL 1200 EX TEM running at 80 kV and digital images were captured using Olympus ITEM software and a Cantega 2kx2k Camera.

Staining and confocal microscopy of human mammary tumors

Human mammary tumors were obtained through NHS Greater Glasgow and Clyde Bio-repository. Formalin-fixed paraffin-embedded tissues were cut into 4 µm thick slices. Nine independent patient samples underwent high-pH antigen retrieval prior to immunofluorescence staining. Samples were permeabilized and blocked with 10% NGS in 1% BSA and 0.3% TX-100 for 30min. Samples were stained with unconjugated anti-TNFRSF12A antibody (1/75, ab109365 Abcam) for 1h in 10% NGS/1% BSA/0.3% TX-100. Samples were washed and stained with the following antibodies: CD31-Alexa Fluor® 488 (1/100, [JC/70A] Abcam), α-SMA-Cy3 (1/1000, [1A4] C6198 Sigma-Aldrich), goat-anti-rabbit Alexa Fluor® 647 (1/200, Invitrogen, Thermo Fisher Scientific) and with Hoescht-33342 (1/5000, Sigma-Aldrich). Samples were mounted with Prolong-Glass Antifade (Invitrogen, Thermo Fisher Scientific) and allowed to cure in the dark for a minimum of 24h prior to imaging. Unstained samples were mounted as auto-fluorescence controls.

Fluorescent samples were imaged using a Zeiss 880 LSM confocal microscope (Carl Zeiss) in Lambda mode with a 32-channel spectral detector, and spectral unmixing was performed to remove as much tissue auto-fluorescence as possible. The auto-fluorescence spectrum was obtained from an unstained control, and fluorescence spectra were obtained from individual dyes (Hoescht, Alexa Fluor-488, Cy3, Alexa Fluor-647) using 405 nm, 488 nm, 561 nm and 647 nm lasers. Unbiased imaging of entire tissue sections was performed using a Plan-Apochromat 20x/0.8 M27 objective using tilescan and Z-stack modes. Tile stitching, maximum Z projection and linear unmixing was performed using Zen Black software (version 2.3 SP1), and images were visualized in Zen Blue software (version 2.3). More detailed imaging of three tissue samples was performed using a Plan-Apochromat 40x/1.3 Oil DIC M27 objective and Z-stack mode. Maximum Z projection and linear unmixing was performed as above. Image processing was performed in Fiji (ImageJ, version 1.53f51).

Reverse transcription polymerase chain reaction (RT-qPCR) analysis

RNA was extracted from cultured cells or cells sorted after co-culture. DNase treatment and total RNA isolation were performed using the RNeasy mini kit (Qiagen) according to the manufacturer's instructions. 1 µg of RNA was used to synthesize complementary DNA using the iScript kit (BioRad). DNA was diluted to 10 ng/µl and 2 µl were used in each RT-qPCR reaction with 10 µl of iTaq Universal SYBR Green Supermix (Bio-Rad Laboratories) and 400 nM of forward and reverse primers. PCR runs were performed using a QuantStudio™ 3 Real-Time PCR System (Thermo Fisher Scientific). Primers are listed in table S1.

Single-cell RNA sequencing

Data were analyzed as described in the original manuscripts [7, 16].

Statistical analysis

Statistical analysis was performed on biologically independent replicates (*N*) using GraphPad Prism software version 9 (GraphPad Software Inc.). A Shapiro-Wilk test has been used to test data for normality, then, the *P* value was calculated as detailed in each figure legend. A $P \leq 0.05$ was considered significant.

Supplementary Materials

Figs. S1 to S8

Table S1

Data files S1 to S6

References and Notes

1. Gerhart, J. (1999) 1998 Warkany lecture: signaling pathways in development, *Teratology.* **60**, 226-39.
2. Pires-daSilva, A. & Sommer, R. J. (2003) The evolution of signalling pathways in animal development, *Nat Rev Genet.* **4**, 39-49.
3. McCrea, P. D., Gu, D. & Balda, M. S. (2009) Junctional music that the nucleus hears: cell-cell contact signaling and the modulation of gene activity, *Cold Spring Harb Perspect Biol.* **1**, a002923.

4. Brucher, B. L. & Jamall, I. S. (2014) Cell-cell communication in the tumor microenvironment, carcinogenesis, and anticancer treatment, *Cell Physiol Biochem.* **34**, 213-43.
5. Brucher, B. L. & Jamall, I. S. (2014) Epistemology of the origin of cancer: a new paradigm, *BMC Cancer.* **14**, 331.
6. Santi, A., Kugeratski, F. G. & Zanivan, S. (2018) Cancer Associated Fibroblasts: The Architects of Stroma Remodeling, *Proteomics.* **18**, e1700167.
7. Wu, S. Z., Roden, D. L., Wang, C., Holliday, H., Harvey, K., Cazet, A. S., Murphy, K. J., Pereira, B., Al-Eryani, G., Bartonicek, N., Hou, R., Torpy, J. R., Junankar, S., Chan, C. L., Lam, C. E., Hui, M. N., Gluch, L., Beith, J., Parker, A., Robbins, E., Segara, D., Mak, C., Cooper, C., Warrier, S., Forrest, A., Powell, J., O'Toole, S., Cox, T. R., Timpson, P., Lim, E., Liu, X. S. & Swarbrick, A. (2020) Stromal cell diversity associated with immune evasion in human triple-negative breast cancer, *EMBO J.* **39**, e104063.
8. Walker, R. A. (2001) The complexities of breast cancer desmoplasia, *Breast Cancer Res.* **3**, 143-5.
9. Nissen, N. I., Karsdal, M. & Willumsen, N. (2019) Collagens and Cancer associated fibroblasts in the reactive stroma and its relation to Cancer biology, *J Exp Clin Cancer Res.* **38**, 115.
10. Marsh, T., Pietras, K. & McAllister, S. S. (2013) Fibroblasts as architects of cancer pathogenesis, *Biochim Biophys Acta.* **1832**, 1070-8.
11. Kalluri, R. (2016) The biology and function of fibroblasts in cancer, *Nat Rev Cancer.* **16**, 582-98.
12. Monteran, L. & Erez, N. (2019) The Dark Side of Fibroblasts: Cancer-Associated Fibroblasts as Mediators of Immunosuppression in the Tumor Microenvironment, *Front Immunol.* **10**, 1835.
13. Sahai, E., Astsaturov, I., Cukierman, E., DeNardo, D. G., Egeblad, M., Evans, R. M., Fearon, D., Greten, F. R., Hingorani, S. R., Hunter, T., Hynes, R. O., Jain, R. K., Janowitz, T., Jorgensen, C., Kimmelman, A. C., Kolonin, M. G., Maki, R. G., Powers, R. S., Puré, E., Ramirez, D. C., Scherz-Shouval, R., Sherman, M. H., Stewart, S., Tlsty, T. D., Tuveson, D. A., Watt, F. M., Weaver, V., Weeraratna, A. T. & Werb, Z. (2020) A framework for advancing our understanding of cancer-associated fibroblasts, *Nat Rev Cancer.* **20**, 174-186.
14. Shoucair, I., Weber Mello, F., Jabalee, J., Maleki, S. & Garnis, C. (2020) The Role of Cancer-Associated Fibroblasts and Extracellular Vesicles in Tumorigenesis, *Int J Mol Sci.* **21**.
15. Biffi, G. & Tuveson, D. A. (2021) Diversity and Biology of Cancer-Associated Fibroblasts, *Physiol Rev.* **101**, 147-176.
16. Kieffer, Y., Hocine, H. R., Gentric, G., Pelon, F., Bernard, C., Bourachot, B., Lameiras, S., Albergante, L., Bonneau, C., Guyard, A., Tarte, K., Zinovyev, A., Baulande, S., Zalcman, G., Vincent-Salomon, A. & Mechta-Grigoriou, F. (2020) Single-Cell Analysis Reveals Fibroblast Clusters Linked to Immunotherapy Resistance in Cancer, *Cancer Discov.* **10**, 1330-1351.
17. Ohlund, D., Handly-Santana, A., Biffi, G., Elyada, E., Almeida, A. S., Ponz-Sarvise, M., Corbo, V., Oni, T. E., Hearn, S. A., Lee, E. J., Chio, I., Hwang, C. I., Tiriac, H., Baker, L. A., Engle, D. D., Feig, C., Kultti, A., Egeblad, M., Fearon, D. T., Crawford, J. M., Clevers, H., Park, Y. & Tuveson, D. A. (2017) Distinct populations of inflammatory fibroblasts and myofibroblasts in pancreatic cancer, *J Exp Med.* **214**, 579-596.
18. Sousa, C. M., Biancur, D. E., Wang, X., Halbrook, C. J., Sherman, M. H., Zhang, L., Kremer, D., Hwang, R. F., Witkiewicz, A. K., Ying, H., Asara, J. M., Evans, R. M., Cantley, L. C., Lyssiotis, C. A. & Kimmelman, A. C. (2016) Pancreatic stellate cells support tumour metabolism through autophagic alanine secretion, *Nature.* **536**, 479-83.
19. Yang, L., Achreja, A., Yeung, T. L., Mangala, L. S., Jiang, D., Han, C., Baddour, J., Marini, J. C., Ni, J., Nakahara, R., Wahlig, S., Chiba, L., Kim, S. H., Morse, J., Pradeep, S., Nagaraja, A. S.,

Haemmerle, M., Kyunghee, N., Derichsweiler, M., Plackemeier, T., Mercado-Uribe, I., Lopez-Berestein, G., Moss, T., Ram, P. T., Liu, J., Lu, X., Mok, S. C., Sood, A. K. & Nagrath, D. (2016) Targeting Stromal Glutamine Synthetase in Tumors Disrupts Tumor Microenvironment-Regulated Cancer Cell Growth, *Cell Metab.* **24**, 685-700.
20. Zhao, H., Yang, L., Baddour, J., Achreja, A., Bernard, V., Moss, T., Marini, J. C., Tudawe, T., Seviour, E. G., San Lucas, F. A., Alvarez, H., Gupta, S., Maiti, S. N., Cooper, L., Peehl, D., Ram, P. T., Maitra, A. & Nagrath, D. (2016) Tumor microenvironment derived exosomes pleiotropically modulate cancer cell metabolism, *Elife.* **5**, e10250.
21. Santi, A., Caselli, A., Ranaldi, F., Paoli, P., Mugnaioni, C., Michelucci, E. & Cirri, P. (2015) Cancer associated fibroblasts transfer lipids and proteins to cancer cells through cargo vesicles supporting tumor growth, *Biochim Biophys Acta.* **1853**, 3211-23.
22. Toti, A., Santi, A., Pardella, E., Nesi, I., Tomasini, R., Mello, T., Paoli, P., Caselli, A. & Cirri, P. (2021) Activated fibroblasts enhance cancer cell migration by microvesicles-mediated transfer of Galectin-1, *J Cell Commun Signal.* **15**, 405-419.
23. Spees, J. L., Olson, S. D., Whitney, M. J. & Prockop, D. J. (2006) Mitochondrial transfer between cells can rescue aerobic respiration, *Proc Natl Acad Sci U S A.* **103**, 1283-8.
24. Ippolito, L., Morandi, A., Taddei, M. L., Parri, M., Comito, G., Iscaro, A., Raspollini, M. R., Magherini, F., Rapizzi, E., Masquelier, J., Muccioli, G. G., Sonveaux, P., Chiarugi, P. & Giannoni, E. (2019) Cancer-associated fibroblasts promote prostate cancer malignancy via metabolic rewiring and mitochondrial transfer, *Oncogene.* **38**, 5339-5355.
25. Davis, D. M. (2007) Intercellular transfer of cell-surface proteins is common and can affect many stages of an immune response, *Nat Rev Immunol.* **7**, 238-43.
26. Smyth, L. A., Afzali, B., Tsang, J., Lombardi, G. & Lechler, R. I. (2007) Intercellular transfer of MHC and immunological molecules: molecular mechanisms and biological significance, *Am J Transplant.* **7**, 1442-9.
27. Rechavi, O., Goldstein, I. & Kloog, Y. (2009) Intercellular exchange of proteins: the immune cell habit of sharing, *FEBS Lett.* **583**, 1792-9.
28. Rechavi, O., Kalman, M., Fang, Y., Vernitsky, H., Jacob-Hirsch, J., Foster, L. J., Kloog, Y. & Goldstein, I. (2010) Trans-SILAC: sorting out the non-cell-autonomous proteome, *Nat Methods.* **7**, 923-7.
29. Ahmed, K. A. & Xiang, J. (2011) Mechanisms of cellular communication through intercellular protein transfer, *J Cell Mol Med.* **15**, 1458-73.
30. Thery, C.Witwer, K. W.Aikawa, E.Alcaraz, M. J.Anderson, J. D.Andriantsitohaina, R.Antoniou, A.Arab, T.Archer, F.Atkin-Smith, G. K.Ayre, D. C.Bach, J. M.Bachurski, D.Baharvand, H.Balaj, L.Baldacchino, S.Bauer, N. N.Baxter, A. A.Bebawy, M.Beckham, C.Bedina Zavec, A.Benmoussa, A.Berardi, A. C.Bergese, P.Bielska, E.Blenkiron, C.Bobis-Wozowicz, S.Boilard, E.Boireau, W.Bongiovanni, A.Borras, F. E.Bosch, S.Boulanger, C. M.Breakefield, X.Breglio, A. M.Brennan, M. A.Brigstock, D. R.Brisson, A.Broekman, M. L.Bromberg, J. F.Bryl-Gorecka, P.Buch, S.Buck, A. H.Burger, D.Busatto, S.Buschmann, D.Bussolati, B.Buzas, E. I.Byrd, J. B.Camussi, G.Carter, D. R.Caruso, S.Chamley, L. W.Chang, Y. T.Chen, C.Chen, S.Cheng, L.Chin, A. R.Clayton, A.Clerici, S. P.Cocks, A.Cocucci, E.Coffey, R. J.Cordeiro-da-Silva, A.Couch, Y.Coumans, F. A.Coyle, B.Crescitelli, R.Criado, M. F.D'Souza-Schorey, C.Das, S.Datta Chaudhuri, A.de Candia, P.De Santana, E. F.De Wever, O.Del Portillo, H. A.Demaret, T.Deville, S.Devitt, A.Dhondt, B.Di Vizio, D.Dieterich, L. C.Dolo, V.Dominguez Rubio, A. P.Dominici, M.Dourado, M. R.Driedonks, T. A.Duarte, F. V.Duncan, H. M.Eichenberger, R. M.Ekstrom, K.El Andaloussi, S.Elie-Caille, C.Erdbrugger, U.Falcon-Perez, J. M.Fatima, F.Fish, J. E.Flores-Bellver, M.Forsonits, A.Frelet-Barrand, A., et al. (2018) Minimal information for studies of extracellular vesicles 2018 (MISEV2018): a position

statement of the International Society for Extracellular Vesicles and update of the MISEV2014 guidelines, *J Extracell Vesicles.* **7**, 1535750.
31. Mathieu, M., Martin-Jaular, L., Lavieu, G. & Thery, C. (2019) Specificities of secretion and uptake of exosomes and other extracellular vesicles for cell-to-cell communication, *Nat Cell Biol.* **21**, 9-17.
32. Huleihel, L., Hussey, G. S., Naranjo, J. D., Zhang, L., Dziki, J. L., Turner, N. J., Stolz, D. B. & Badylak, S. F. (2016) Matrix-bound nanovesicles within ECM bioscaffolds, *Sci Adv.* **2**, e1600502.
33. Hussey, G. S., Pineda Molina, C., Cramer, M. C., Tyurina, Y. Y., Tyurin, V. A., Lee, Y. C., El-Mossier, S. O., Murdock, M. H., Timashev, P. S., Kagan, V. E. & Badylak, S. F. (2020) Lipidomics and RNA sequencing reveal a novel subpopulation of nanovesicle within extracellular matrix biomaterials, *Sci Adv.* **6**, eaay4361.
34. Huleihel, L., Bartolacci, J. G., Dziki, J. L., Vorobyov, T., Arnold, B., Scarritt, M. E., Pineda Molina, C., LoPresti, S. T., Brown, B. N., Naranjo, J. D. & Badylak, S. F. (2017) Matrix-Bound Nanovesicles Recapitulate Extracellular Matrix Effects on Macrophage Phenotype, *Tissue Eng Part A.* **23**, 1283-1294.
35. Kay, E. J., Paterson, K., Riera-Domingo, C., Sumpton, D., Däbritz, J. H. M., Tardito, S., Boldrini, C., Hernandez-Fernaud, J. R., Athineos, D., Dhayade, S., Stepanova, E., Gjerga, E., Neilson, L. J., Lilla, S., Hedley, A., Koulouras, G., McGregor, G., Jamieson, C., Johnson, R. M., Park, M., Kirschner, K., Miller, C., Kamphorst, J. J., Loayza-Puch, F., Saez-Rodriguez, J., Mazzone, M., Blyth, K., Zagnoni, M. & Zanivan, S. (2022) Cancer-associated fibroblasts require proline synthesis by PYCR1 for the deposition of pro-tumorigenic extracellular matrix, *Nat Metab.* **4**, 693-710.
36. LeBleu, V. S., Teng, Y., O'Connell, J. T., Charytan, D., Muller, G. A., Muller, C. A., Sugimoto, H. & Kalluri, R. (2013) Identification of human epididymis protein-4 as a fibroblast-derived mediator of fibrosis, *Nat Med.* **19**, 227-31.
37. Venning, F. A., Zornhagen, K. W., Wullkopf, L., Sjolund, J., Rodriguez-Cupello, C., Kjellman, P., Morsing, M., Hajkarim, M. C., Won, K. J., Erler, J. T. & Madsen, C. D. (2021) Deciphering the temporal heterogeneity of cancer-associated fibroblast subpopulations in breast cancer, *J Exp Clin Cancer Res.* **40**, 175.
38. Rautou, P. E., Leroyer, A. S., Ramkhelawon, B., Devue, C., Duflaut, D., Vion, A. C., Nalbone, G., Castier, Y., Leseche, G., Lehoux, S., Tedgui, A. & Boulanger, C. M. (2011) Microparticles from human atherosclerotic plaques promote endothelial ICAM-1-dependent monocyte adhesion and transendothelial migration, *Circ Res.* **108**, 335-43.
39. Huang, A., Dong, J., Li, S., Wang, C., Ding, H., Li, H., Su, X., Ge, X., Sun, L., Bai, C., Shen, X., Fang, T., Li, J. & Shao, N. (2015) Exosomal transfer of vasorin expressed in hepatocellular carcinoma cells promotes migration of human umbilical vein endothelial cells, *Int J Biol Sci.* **11**, 961-9.
40. Kannan, K., Stewart, R. M., Bounds, W., Carlsson, S. R., Fukuda, M., Betzing, K. W. & Holcombe, R. F. (1996) Lysosome-associated membrane proteins h-LAMP1 (CD107a) and h-LAMP2 (CD107b) are activation-dependent cell surface glycoproteins in human peripheral blood mononuclear cells which mediate cell adhesion to vascular endothelium, *Cell Immunol.* **171**, 10-9.
41. Sarafian, V., Jadot, M., Foidart, J. M., Letesson, J. J., Van den Brule, F., Castronovo, V., Wattiaux, R. & Coninck, S. W. (1998) Expression of Lamp-1 and Lamp-2 and their interactions with galectin-3 in human tumor cells, *Int J Cancer.* **75**, 105-11.
42. Dedieu, S. & Langlois, B. (2008) LRP-1: a new modulator of cytoskeleton dynamics and adhesive complex turnover in cancer cells, *Cell Adh Migr.* **2**, 77-80.

43. Min, B. K., Suk, K. & Lee, W. H. (2013) Stimulation of CD107 affects LPS-induced cytokine secretion and cellular adhesion through the ERK signaling pathway in the human macrophage-like cell line, THP-1, *Cell Immunol.* **281**, 122-8.
44. Potere, N., Del Buono, M. G., Mauro, A. G., Abbate, A. & Toldo, S. (2019) Low Density Lipoprotein Receptor-Related Protein-1 in Cardiac Inflammation and Infarct Healing, *Front Cardiovasc Med.* **6**, 51.
45. Herrera-Molina, R., Valdivia, A., Kong, M., Alvarez, A., Cardenas, A., Quest, A. F. & Leyton, L. (2013) Thy-1-interacting molecules and cellular signaling in cis and trans, *Int Rev Cell Mol Biol.* **305**, 163-216.
46. Fiore, V. F., Ju, L., Chen, Y., Zhu, C. & Barker, T. H. (2014) Dynamic catch of a Thy-1-alpha5beta1+syndecan-4 trimolecular complex, *Nat Commun.* **5**, 4886.
47. Luster, A. D., Alon, R. & von Andrian, U. H. (2005) Immune cell migration in inflammation: present and future therapeutic targets, *Nat Immunol.* **6**, 1182-90.
48. Shen, X., Wang, C., Zhu, H., Wang, Y., Wang, X., Cheng, X., Ge, W. & Lu, W. (2021) Exosome-mediated transfer of CD44 from high-metastatic ovarian cancer cells promotes migration and invasion of low-metastatic ovarian cancer cells, *J Ovarian Res.* **14**, 38.
49. Saalbach, A., Haustein, U. F. & Anderegg, U. (2000) A ligand of human thy-1 is localized on polymorphonuclear leukocytes and monocytes and mediates the binding to activated thy-1-positive microvascular endothelial cells and fibroblasts, *J Invest Dermatol.* **115**, 882-8.
50. Wetzel, A., Chavakis, T., Preissner, K. T., Sticherling, M., Haustein, U. F., Anderegg, U. & Saalbach, A. (2004) Human Thy-1 (CD90) on activated endothelial cells is a counterreceptor for the leukocyte integrin Mac-1 (CD11b/CD18), *J Immunol.* **172**, 3850-9.
51. Wetzel, A., Wetzig, T., Haustein, U. F., Sticherling, M., Anderegg, U., Simon, J. C. & Saalbach, A. (2006) Increased neutrophil adherence in psoriasis: role of the human endothelial cell receptor Thy-1 (CD90), *J Invest Dermatol.* **126**, 441-52.
52. Schliekelman, M. J., Creighton, C. J., Baird, B. N., Chen, Y., Banerjee, P., Bota-Rabassedas, N., Ahn, Y. H., Roybal, J. D., Chen, F., Zhang, Y., Mishra, D. K., Kim, M. P., Liu, X., Mino, B., Villalobos, P., Rodriguez-Canales, J., Behrens, C., Wistuba, I. I., Hanash, S. M. & Kurie, J. M. (2017) Thy-1, *Sci Rep.* **7**, 6478.
53. Elyada, E., Bolisetty, M., Laise, P., Flynn, W. F., Courtois, E. T., Burkhart, R. A., Teinor, J. A., Belleau, P., Biffi, G., Lucito, M. S., Sivajothi, S., Armstrong, T. D., Engle, D. D., Yu, K. H., Hao, Y., Wolfgang, C. L., Park, Y., Preall, J., Jaffee, E. M., Califano, A., Robson, P. & Tuveson, D. A. (2019) Cross-Species Single-Cell Analysis of Pancreatic Ductal Adenocarcinoma Reveals Antigen-Presenting Cancer-Associated Fibroblasts, *Cancer Discov.* **9**, 1102-1123.
54. Singh, A., Fedele, C., Lu, H., Nevalainen, M. T., Keen, J. H. & Languino, L. R. (2016) Exosome-mediated Transfer of alphavbeta3 Integrin from Tumorigenic to Nontumorigenic Cells Promotes a Migratory Phenotype, *Mol Cancer Res.* **14**, 1136-1146.
55. Nakamura, K., Sawada, K., Kinose, Y., Yoshimura, A., Toda, A., Nakatsuka, E., Hashimoto, K., Mabuchi, S., Morishige, K. I., Kurachi, H., Lengyel, E. & Kimura, T. (2017) Exosomes Promote Ovarian Cancer Cell Invasion through Transfer of CD44 to Peritoneal Mesothelial Cells, *Mol Cancer Res.* **15**, 78-92.
56. Kugeratski, F. G., Hodge, K., Lilla, S., McAndrews, K. M., Zhou, X., Hwang, R. F., Zanivan, S. & Kalluri, R. (2021) Quantitative proteomics identifies the core proteome of exosomes with syntenin-1 as the highest abundant protein and a putative universal biomarker, *Nat Cell Biol.* **23**, 631-641.

57. Xu, R., Greening, D. W., Rai, A., Ji, H. & Simpson, R. J. (2015) Highly-purified exosomes and shed microvesicles isolated from the human colon cancer cell line LIM1863 by sequential centrifugal ultrafiltration are biochemically and functionally distinct, *Methods.* **87**, 11-25.
58. Minciacchi, V. R., You, S., Spinelli, C., Morley, S., Zandian, M., Aspuria, P. J., Cavallini, L., Ciardiello, C., Reis Sobreiro, M., Morello, M., Kharmate, G., Jang, S. C., Kim, D. K., Hosseini-Beheshti, E., Tomlinson Guns, E., Gleave, M., Gho, Y. S., Mathivanan, S., Yang, W., Freeman, M. R. & Di Vizio, D. (2015) Large oncosomes contain distinct protein cargo and represent a separate functional class of tumor-derived extracellular vesicles, *Oncotarget.* **6**, 11327-41.
59. Kowal, J., Arras, G., Colombo, M., Jouve, M., Morath, J. P., Primdal-Bengtson, B., Dingli, F., Loew, D., Tkach, M. & Thery, C. (2016) Proteomic comparison defines novel markers to characterize heterogeneous populations of extracellular vesicle subtypes, *Proc Natl Acad Sci U S A.* **113**, E968-77.
60. Belhabib, I., Zaghdoudi, S., Lac, C., Bousquet, C. & Jean, C. (2021) Extracellular Matrices and Cancer-Associated Fibroblasts: Targets for Cancer Diagnosis and Therapy?, *Cancers (Basel).* **13**.
61. Sebastian, A., Hum, N. R., Martin, K. A., Gilmore, S. F., Peran, I., Byers, S. W., Wheeler, E. K., Coleman, M. A. & Loots, G. G. (2020) Single-Cell Transcriptomic Analysis of Tumor-Derived Fibroblasts and Normal Tissue-Resident Fibroblasts Reveals Fibroblast Heterogeneity in Breast Cancer, *Cancers (Basel).* **12**.
62. Pedrioli, G. & Paganetti, P. (2020) Hijacking Endocytosis and Autophagy in Extracellular Vesicle Communication: Where the Inside Meets the Outside, *Front Cell Dev Biol.* **8**, 595515.
63. Gurung, S., Perocheau, D., Touramanidou, L. & Baruteau, J. (2021) The exosome journey: from biogenesis to uptake and intracellular signalling, *Cell Commun Signal.* **19**, 47.
64. Zheng, J., Tan, J., Miao, Y. Y. & Zhang, Q. (2019) Extracellular vesicles degradation pathway based autophagy lysosome pathway, *Am J Transl Res.* **11**, 1170-1183.
65. Kim, I. S., Gao, Y., Welte, T., Wang, H., Liu, J., Janghorban, M., Sheng, K., Niu, Y., Goldstein, A., Zhao, N., Bado, I., Lo, H. C., Toneff, M. J., Nguyen, T., Bu, W., Jiang, W., Arnold, J., Gu, F., He, J., Jebakumar, D., Walker, K., Li, Y., Mo, Q., Westbrook, T. F., Zong, C., Rao, A., Sreekumar, A., Rosen, J. M. & Zhang, X. H. (2019) Immuno-subtyping of breast cancer reveals distinct myeloid cell profiles and immunotherapy resistance mechanisms, *Nat Cell Biol.* **21**, 1113-1126.
66. Kaushik, S., Pickup, M. W. & Weaver, V. M. (2016) From transformation to metastasis: deconstructing the extracellular matrix in breast cancer, *Cancer Metastasis Rev.* **35**, 655-667.
67. Reid, S. E., Kay, E. J., Neilson, L. J., Henze, A. T., Serneels, J., McGhee, E. J., Dhayade, S., Nixon, C., Mackey, J. B., Santi, A., Swaminathan, K., Athineos, D., Papalazarou, V., Patella, F., Roman-Fernandez, A., ElMaghloob, Y., Hernandez-Fernaud, J. R., Adams, R. H., Ismail, S., Bryant, D. M., Salmeron-Sanchez, M., Machesky, L. M., Carlin, L. M., Blyth, K., Mazzone, M. & Zanivan, S. (2017) Tumor matrix stiffness promotes metastatic cancer cell interaction with the endothelium, *EMBO J.* **36**, 2373-2389.
68. Winkler, J., Abisoye-Ogunniyan, A., Metcalf, K. J. & Werb, Z. (2020) Concepts of extracellular matrix remodelling in tumour progression and metastasis, *Nat Commun.* **11**, 5120.
69. Albacete-Albacete, L., Navarro-Lerida, I., Lopez, J. A., Martin-Padura, I., Astudillo, A. M., Ferrarini, A., Van-Der-Heyden, M., Balsinde, J., Orend, G., Vazquez, J. & Del Pozo, M. A. (2020) ECM deposition is driven by caveolin-1-dependent regulation of exosomal biogenesis and cargo sorting, *J Cell Biol.* **219**.
70. Nawaz, M., Shah, N., Zanetti, B. R., Maugeri, M., Silvestre, R. N., Fatima, F., Neder, L. & Valadi, H. (2018) Extracellular Vesicles and Matrix Remodeling Enzymes: The Emerging Roles in Extracellular Matrix Remodeling, Progression of Diseases and Tissue Repair, *Cells.* **7**.

71. Sung, B. H., Ketova, T., Hoshino, D., Zijlstra, A. & Weaver, A. M. (2015) Directional cell movement through tissues is controlled by exosome secretion, *Nat Commun.* **6**, 7164.
72. O'Brien, K., Ughetto, S., Mahjoum, S., Nair, A. V. & Breakefield, X. O. (2022) Uptake, functionality, and re-release of extracellular vesicle-encapsulated cargo, *Cell Rep.* **39**, 110651.
73. Becker, A., Thakur, B. K., Weiss, J. M., Kim, H. S., Peinado, H. & Lyden, D. (2016) Extracellular Vesicles in Cancer: Cell-to-Cell Mediators of Metastasis, *Cancer Cell.* **30**, 836-848.
74. Hosios, A. M., Hecht, V. C., Danai, L. V., Johnson, M. O., Rathmell, J. C., Steinhauser, M. L., Manalis, S. R. & Vander Heiden, M. G. (2016) Amino Acids Rather than Glucose Account for the Majority of Cell Mass in Proliferating Mammalian Cells, *Dev Cell.* **36**, 540-9.
75. Commisso, C., Davidson, S. M., Soydaner-Azeloglu, R. G., Parker, S. J., Kamphorst, J. J., Hackett, S., Grabocka, E., Nofal, M., Drebin, J. A., Thompson, C. B., Rabinowitz, J. D., Metallo, C. M., Vander Heiden, M. G. & Bar-Sagi, D. (2013) Macropinocytosis of protein is an amino acid supply route in Ras-transformed cells, *Nature.* **497**, 633-7.
76. Lin, X. P., Mintern, J. D. & Gleeson, P. A. (2020) Macropinocytosis in Different Cell Types: Similarities and Differences, *Membranes (Basel).* **10**.
77. Li, X., Sun, X. & Carmeliet, P. (2019) Hallmarks of Endothelial Cell Metabolism in Health and Disease, *Cell Metab.* **30**, 414-433.
78. Comito, G., Ippolito, L., Chiarugi, P. & Cirri, P. (2020) Nutritional Exchanges Within Tumor Microenvironment: Impact for Cancer Aggressiveness, *Front Oncol.* **10**, 396.
79. Bergers, G. & Song, S. (2005) The role of pericytes in blood-vessel formation and maintenance, *Neuro Oncol.* **7**, 452-64.
80. Latif, N., Sarathchandra, P., Chester, A. H. & Yacoub, M. H. (2015) Expression of smooth muscle cell markers and co-activators in calcified aortic valves, *Eur Heart J.* **36**, 1335-45.
81. Alvarez-Castelao, B., Schanzenbacher, C. T., Hanus, C., Glock, C., Tom Dieck, S., Dorrbaum, A. R., Bartnik, I., Nassim-Assir, B., Ciirdaeva, E., Mueller, A., Dieterich, D. C., Tirrell, D. A., Langer, J. D. & Schuman, E. M. (2017) Cell-type-specific metabolic labeling of nascent proteomes in vivo, *Nat Biotechnol.* **35**, 1196-1201.
82. Kojima, Y., Acar, A., Eaton, E. N., Mellody, K. T., Scheel, C., Ben-Porath, I., Onder, T. T., Wang, Z. C., Richardson, A. L., Weinberg, R. A. & Orimo, A. (2010) Autocrine TGF-beta and stromal cell-derived factor-1 (SDF-1) signaling drives the evolution of tumor-promoting mammary stromal myofibroblasts, *Proc Natl Acad Sci U S A.* **107**, 20009-14.
83. Aper, S. J., van Spreeuwel, A. C., van Turnhout, M. C., van der Linden, A. J., Pieters, P. A., van der Zon, N. L., de la Rambelje, S. L., Bouten, C. V. & Merkx, M. (2014) Colorful protein-based fluorescent probes for collagen imaging, *PLoS One.* **9**, e114983.
84. Rappsilber, J., Ishihama, Y. & Mann, M. (2003) Stop and go extraction tips for matrix-assisted laser desorption/ionization, nanoelectrospray, and LC/MS sample pretreatment in proteomics, *Anal Chem.* **75**, 663-70.
85. Wisniewski, J. R., Zougman, A., Nagaraj, N. & Mann, M. (2009) Universal sample preparation method for proteome analysis, *Nat Methods.* **6**, 359-62.
86. Kugeratski, F. G., Atkinson, S. J., Neilson, L. J., Lilla, S., Knight, J. R. P., Serneels, J., Juin, A., Ismail, S., Bryant, D. M., Markert, E. K., Machesky, L. M., Mazzone, M., Sansom, O. J. & Zanivan, S. (2019) Hypoxic cancer-associated fibroblasts increase NCBP2-AS2/HIAR to promote endothelial sprouting through enhanced VEGF signaling, *Sci Signal.* **12**.
87. Shevchenko, A., Tomas, H., Havlis, J., Olsen, J. V. & Mann, M. (2006) In-gel digestion for mass spectrometric characterization of proteins and proteomes, *Nat Protoc.* **1**, 2856-60.
88. Tyanova, S., Temu, T. & Cox, J. (2016) The MaxQuant computational platform for mass spectrometry-based shotgun proteomics, *Nat Protoc.* **11**, 2301-2319.

89. Tyanova, S., Temu, T., Sinitcyn, P., Carlson, A., Hein, M. Y., Geiger, T., Mann, M. & Cox, J. (2016) The Perseus computational platform for comprehensive analysis of (prote)omics data, *Nat Methods.* **13**, 731-40.
90. Li, W., Germain, R. N. & Gerner, M. Y. (2019) High-dimensional cell-level analysis of tissues with Ce3D multiplex volume imaging, *Nat Protoc.* **14**, 1708-1733.
91. Vizcaino, J. A., Cote, R. G., Csordas, A., Dianes, J. A., Fabregat, A., Foster, J. M., Griss, J., Alpi, E., Birim, M., Contell, J., O'Kelly, G., Schoenegger, A., Ovelleiro, D., Perez-Riverol, Y., Reisinger, F., Rios, D., Wang, R. & Hermjakob, H. (2013) The PRoteomics IDEntifications (PRIDE) database and associated tools: status in 2013, *Nucleic Acids Res.* **41**, D1063-9.

Acknowledgments: We thank Tom Gilbey, the BSU and BAIR at the Cancer Research UK Scotland Institute for providing assistance and technical support. We thank Professor Chiara Bocci (Università degli Studi di Firenze, Italy) for assisting with statistical analysis. In addition, we thank NHS Greater Glasgow and Clyde Bio-repository for providing patient samples and the PRIDE Team. AS has an additional affiliation: Department of Experimental and Clinical Biomedical Sciences, Università degli Studi di Firenze, viale Morgagni 50, 50134 Firenze, Italy. **Funding**: This work was funded by Cancer Research UK Scotland Institute grant A31287; Cancer Research UK Glasgow Centre grant A18076; Cancer Research UK Beatson Institute Advanced Technology Facilities A17196; Stand Up to Cancer campaign for Cancer Research UK grant A29800 to SZ; Cancer Research UK grant A29799 to KB and A23983 to LMC; Breast Cancer Now project grant 2019AugPR1307 to SZ and 2019DecPR1424 to FF and LMC. **Author contributions**: Conceptualization (AS, SZ); Methodology (AS, EJK, LJN, SL, MM, NRP, FF, GK, GRB, DA, SM, MH, GT, YK, LMC); Investigation (AS, EJK, LJN, LM, MM, NRP, YK); Visualization (AS, EJK, LJN, GK, NRP); Supervision (FM-G, CN, KB, LMC, SZ); Writing—original draft (AS); Writing—review & editing (AS, EJK, LMC, SZ). **Competing interests**: The authors declare that they have no competing interests. **Data and materials availability**: The raw files and the MaxQuant search result files have been deposited to the ProteomeXchange Consortium via the PRIDE partner repository [91] with the dataset identifier PXD034450 (proteins transferred from cancer-associated fibroblasts to

endothelial cells: trans-SILAC), PXD034460 (THP-1 proteome), PXD034467 (proteomic analysis of CM-EVs and MBVs secreted by pCAFs), PXD034519 (proteomic analysis of pCAFs expressing high and low α-SMA protein amounts), PXD034573 (pCAF1 proteome), PXD049116 (pCAF/pNF proteome). The pCAF/pNF cell lines were isolated from patient samples obtained from NHS Greater Glasgow and Clyde Biorepository. These cell lines and some information contained in the anonymized pathological report and clinical data can be shared with third party under a Glasgow University MTA. All other data needed to evaluate the conclusions in the paper are present in the paper or the Supplementary Materials.

Figure Legends

Fig. 1

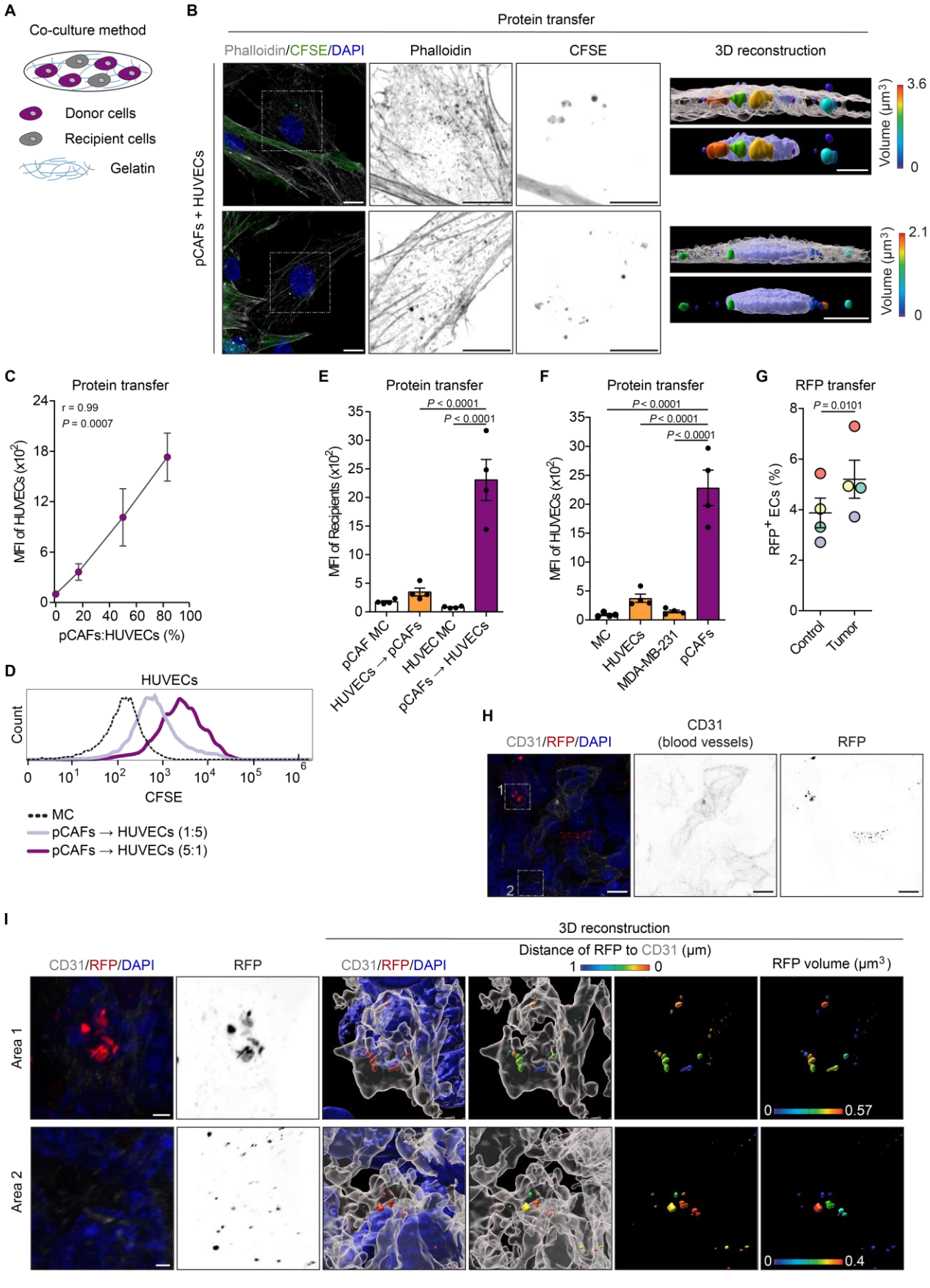

Fig. 1. CAFs transfer proteins to ECs in vitro and in vivo. (A) The direct co-culture method used in Fig. 1B-F. **(B)** Representative images (maximum intensity projection processing from confocal z-stack) and corresponding 3D reconstruction of protein transfer from CFSE-labeled pCAFs (fully green cells) to HUVECs. Actin and nuclei were stained with phalloidin and DAPI, respectively (scale bar = 10 µm). **(C, D)** Quantification (C) of the protein transfer from pCAFs to HUVECs at different ratios between the two cell types. pCAFs:HUVECs ratios are 1:5, 1:1, 5:1. *N* = 3 biological replicates (MFI, median fluorescence intensity and r, Pearson correlation). Representative histogram (D) of the 1:5 and 5:1 ratio. The y-axis is normalized to mode (MC, monoculture). **(E)** Comparison of the protein transfer from HUVECs to pCAFs and from pCAFs to HUVECs. *N* = 4 biological replicates per condition. **(F)** Comparison of the protein transfer from HUVECs to HUVECs, from pCAFs to HUVECs, and from MDA-MB-231 cells to HUVECs. *N* = 4 biological replicates per condition. **(G)** Proportions of RFP^+ ECs ($CD31^+CD45^-$ cells) in the lungs of α-SMA-RFP tumor-free mice or mice with lung metastases. *N* = 4 mice per condition. Paired mice were born on the same day and are indicated with the same color. **(H)** Representative image (maximum intensity projection processing from confocal z-stack) of the tumor area in the lung of α-SMA-RFP mice stained for CD31. Nuclei were stained with DAPI. Scale bar = 10 µm. Representative of 2 mice. **(I)** 3D reconstruction of the tumor vasculature and of the RFP signal; the distance between the RFP signal and the endothelium, and the volume of the RFP signal are shown, scale bar = 2 µm. Representative of 2 mice. Data are presented as means ± standard error of the mean (SEM). One-way ANOVA with Tukey's multiple comparison test for (E, F) and two-tailed paired *t*-test for (G). All significant *P* values are included in the figure.

Fig. 2

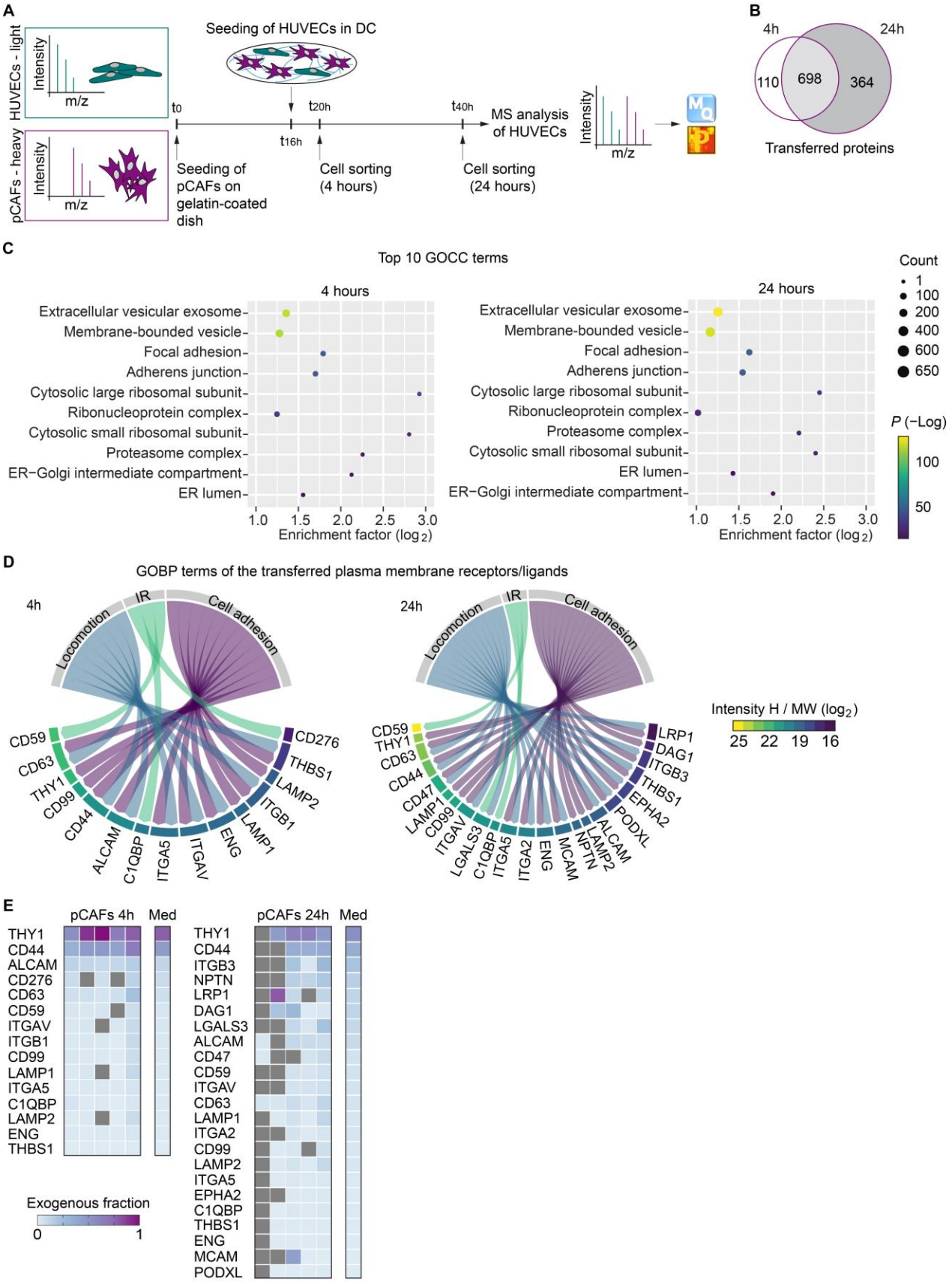
A
HUVECs - light
pCAFs - heavy
Intensity
m/z
Seeding of HUVECs in DC
t0
t16h
t20h
t40h
MS analysis of HUVECs
Seeding of pCAFs on gelatin-coated dish
Cell sorting (4 hours)
Cell sorting (24 hours)
B
4h
24h
110
698
364
Transferred proteins
C
Top 10 GOCC terms
4 hours
24 hours
Extracellular vesicular exosome
Membrane-bounded vesicle
Focal adhesion
Adherens junction
Cytosolic large ribosomal subunit
Ribonucleoprotein complex
Cytosolic small ribosomal subunit
Proteasome complex
ER−Golgi intermediate compartment
ER lumen
Enrichment factor (log2)
Count
P (−Log)
D
GOBP terms of the transferred plasma membrane receptors/ligands
4h
24h
Locomotion
IR
Cell adhesion
Intensity H / MW (log2)
E
pCAFs 4h
Med
pCAFs 24h
Exogenous fraction

Fig. 2. Identification of the proteins transferred from CAFs to ECs. (A) Workflow diagram of the trans-SILAC experiment to identify proteins transferred from pCAFs to HUVECs (DC, direct co-culture). *N* = 5 biological replicates per condition. **(B)** Venn diagram showing the number of transferred proteins at each time point. **(C)** Top 10 GOCC terms based on descending *P* (–Log) and with at least a two-fold enrichment. The enrichment analysis of the transferred proteins was performed using the pCAF proteome (Data File S6) as reference (Fisher exact test). **(D)** Classification of the plasma membrane receptors/ligands based on the GO biological process (GOBP) terms. Proteins are sorted by decreasing values of the median of the intensity value in the "heavy" channel of the trans-SILAC experiment (Intensity H) divided by the MW in the $\log_2$ scale (IR, immune response). **(E)** Heatmap showing the exogenous fraction of the transferred receptors/ligands for each independent experiment and their median. Proteins are sorted by decreasing values of the median of the exogenous fraction.

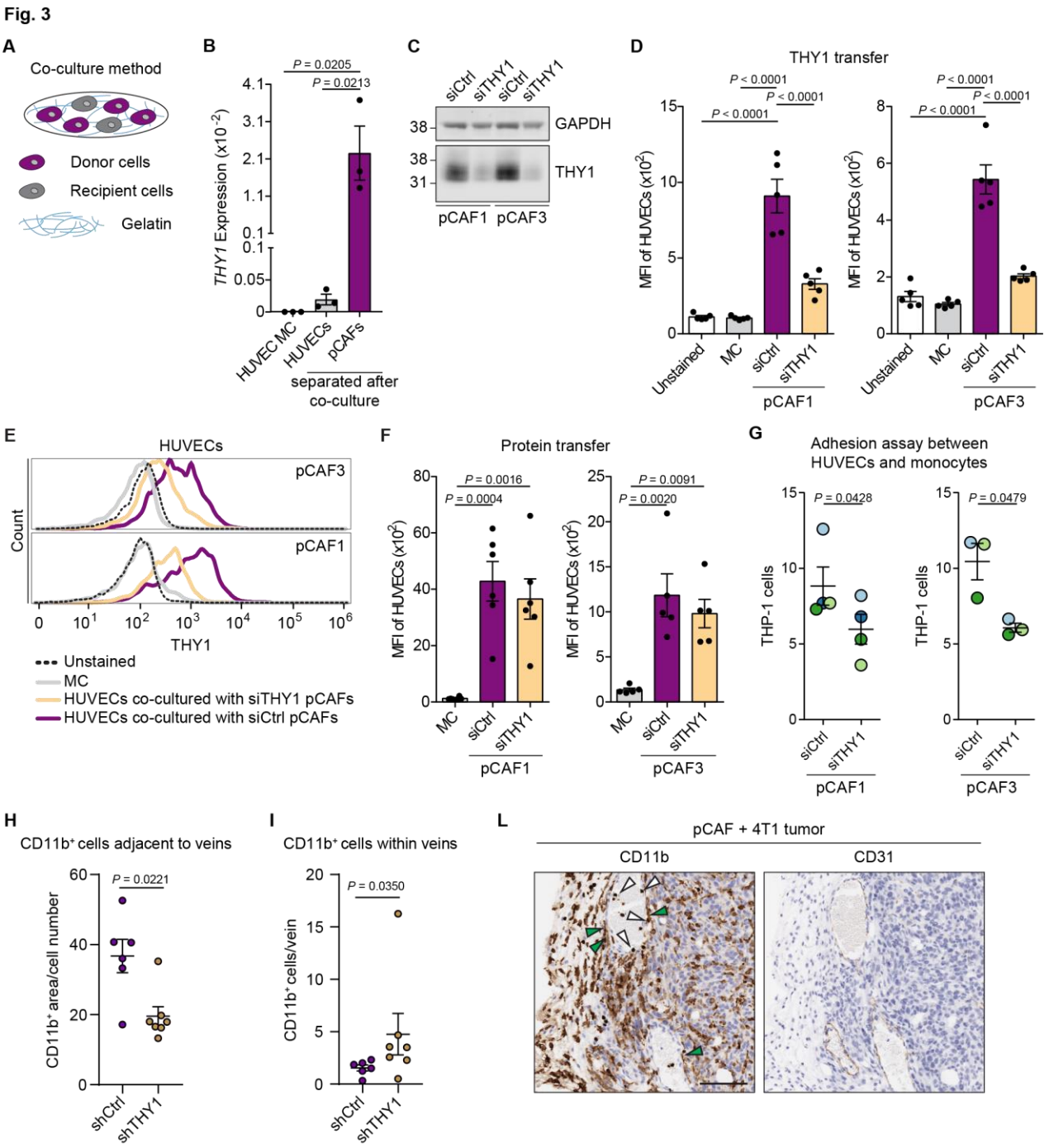

Fig. 3. CAF-derived THY1 supports the physical interaction between ECs and monocytes. (A) The direct co-culture method used in Fig. 3B and D-G. **(B)** mRNA expression of *THY1* in HUVECs in monoculture and after 24h of co-culture with pCAFs and in pCAFs. *THY1* mRNA amount was normalized to *18S* expression. *N* = 3 biological replicates per condition. **(C)** Representative Western blot showing THY1 protein abundance in pCAFs transfected with siCtrl or siTHY1. GAPDH was used as loading control. **(D, E)** Quantification (D) of THY1 protein abundance in monoculture

of HUVECs and HUVECs that were co-cultured with pCAFs transfected with siCtrl or siTHY1 (*N* = 5 biological replicates per condition). Representative histogram (E) of THY1 protein amounts in HUVECs (the y-axis is normalized to mode). **(F)** Quantification of the protein transfer from pCAFs transfected with siCtrl or siTHY1 to HUVECs, *N* = 6 biological replicates for pCAF1 and 5 biological replicates for pCAF3. **(G)** Number of THP-1 monocytes per field bound to HUVECs that were co-cultured with pCAFs silenced or not for THY1. Colors indicate the paired independent experiments. *N* = 4 biological replicates for pCAF1 and 3 biological replicates for pCAF3. **(H)** Quantification of $CD11b^+$ areas adjacent to veins in 4T1 tumors co-transplanted with pCAF1 transfected with shCtrl or shTHY1. *N* = 6 mice for shCtrl and *N* = 7 mice for shTHY1 condition. **(I)** Quantification of $CD11b^+$ cells within veins in 4T1 tumors co-transplanted with pCAF1 transfected with shCtrl or shTHY1. *N* = 6 mice for shCtrl and *N* = 7 mice for the shTHY1 condition. **(L)** Representative images of tumor tissue sections from tumors containing shCtrl-transfected pCAFs stained for CD11b and CD31. The white arrowheads indicate $CD11b^+$ cells within veins; the green arrowheads indicate the areas adjacent to veins where CD11b staining has been quantified. Scale bar = 100 µm. Images are representative of 6 mice. Data are presented as means ± SEM. One-way ANOVA with Tukey's multiple comparison test for (B, D, F), two-tailed paired *t*-test for (G) and two-tailed Mann-Whitney U test for (H, I). All significant *P* values are in the figure.

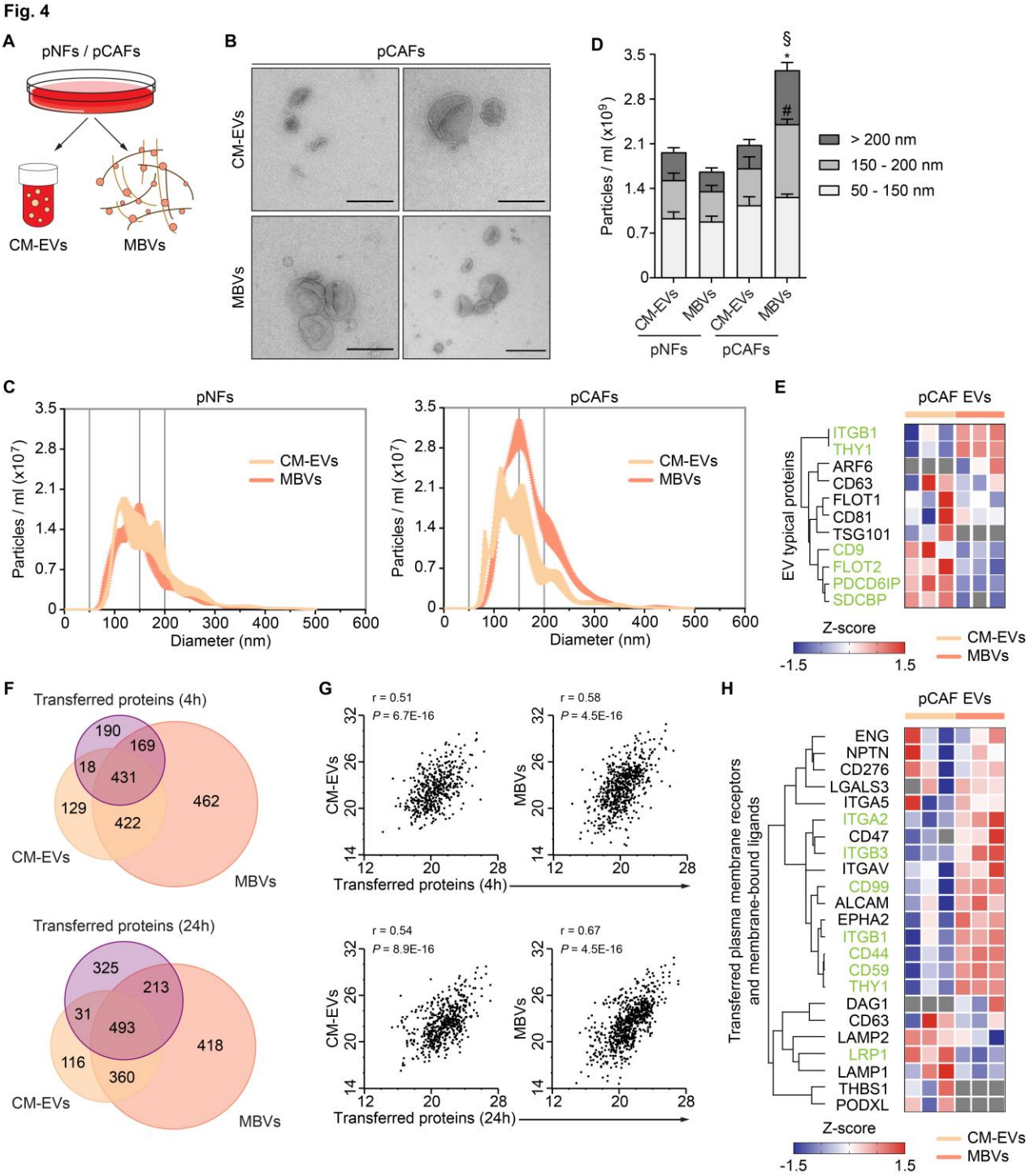

Fig. 4. CAF-derived EVs are carriers of the transferred proteins. (A) Schematic representation of the purified EV types. **(B)** Representative electron microscopy images of pCAF-derived CM-EVs and MBVs. Scale bar = 200 nm. **(C, D)** Frequency plot (C) and histogram (D) showing the total amount and size distribution profile of the CM-EVs and MBVs secreted by pNFs and pCAFs using nanoparticle tracking analysis. *N* = 3 biological replicates per condition. Data are presented as

means ± SEM. * $P \leq 0.05$ between pCAF-derived MBVs and pNF-derived CM-EVs or MBVs or pCAF-derived CM-EVs for the >200 nm fraction. # $P \leq 0.05$ between pCAF-derived MBVs and pNF-derived MBVs or pCAF-derived CM-EVs for the 150–200 nm fraction. § $P \leq 0.05$ between the total amount of pCAF-derived MBVs compared to pNF-derived CM-EVs or MBVs. *P* values were determined by one-way ANOVA with Tukey's multiple comparison test and all significant *P* values are included in the figure. **(E)** Hierarchical clustering based on average Euclidean distance and heatmap based on the Z-score of the LFQ intensity (log_2) calculated for the EV proteins in the EV proteome. Green indicates proteins with significant differences in abundance. $P < 0.05$ by two-tailed *t*-test. $N = 3$ biological replicates per EV type. **(F)** Venn diagram (based on the protein gene names) of the transferred proteins (purple circle) and of the proteins identified by MS proteomics in CM-EVs (light pink circle) and MBVs (dark pink circle). $N = 5$ biological replicates per condition (trans-SILAC experiment) and 3 biological replicates per EV type. **(G)** Scatter plot showing the correlation between the amount of the transferred proteins and their relative content in CM-EVs and MBVs. The y- and x-axis show the median of the intensity divided by MW in the log_2 scale (r, Pearson correlation). $N = 5$ biological replicates per condition (trans-SILAC experiment) and 3 biological replicates per EV type. **(H)** Hierarchical clustering based on average Euclidean distance and heatmap based on the Z-score of the LFQ intensity (log_2) calculated for the transferred plasma membrane receptors and membrane-bound ligands in the EV proteome. Green indicates proteins with significant differences in abundance. $P < 0.05$ by two-tailed *t*-test. $N = 3$ biological replicates per EV type.

Fig. 5

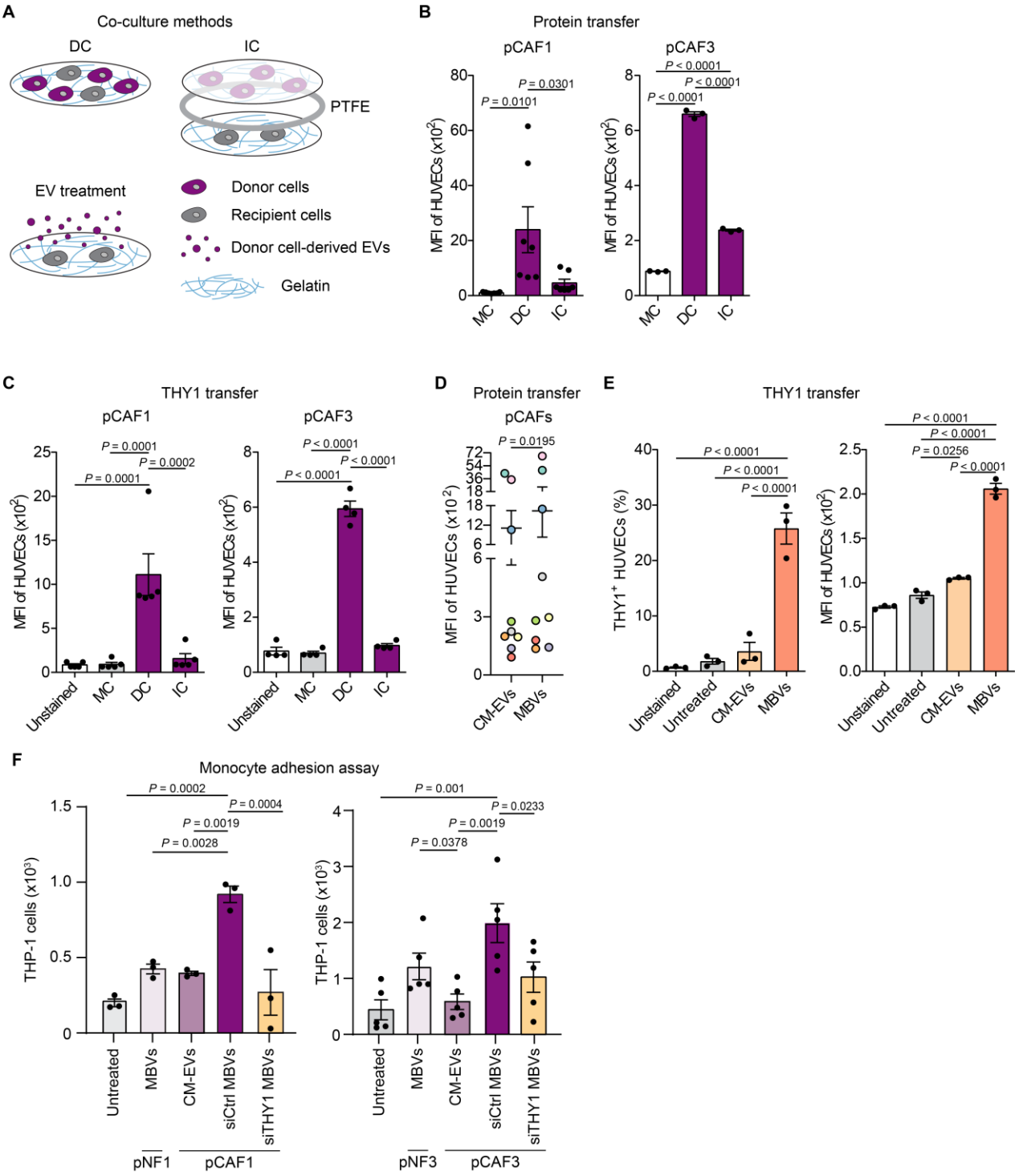

Fig. 5. MBVs have a central role in the protein transfer. (A) The direct (DC) and indirect (IC) co-culture methods used in Fig. 5B-C. pNF- or pCAF-derived EVs were used to treat HUVECs in Fig. 5D-F. **(B)** Quantification of the protein transfer from pCAFs to HUVECs in direct and indirect co-cultures. *N* = 7 biological replicates for pCAF1 and 3 biological replicates for pCAF3. **(C)**

Quantification of THY1 protein abundance in monoculture of HUVECs and HUVECs that were directly and indirectly co-cultured with pCAFs, *N* = 5 biological replicates for pCAF1 and 4 biological replicates for pCAF3. **(D)** Quantification of the amount of proteins transferred by pCAF-derived CM-EVs and MBVs to HUVECs. The EV amount was derived from the same number of donor cells. Colors indicate paired independent experiments. *N* = 9 biological replicates per EV type. Data are normalized to the MFI of the monoculture of HUVECs. The data related to pCAF-derived MBVs also are shown in Fig. 6C. **(E)** Quantification of $THY1^+$ HUVECs and THY1 protein abundance in untreated HUVECs and in HUVECs treated with pCAF-derived CM-EVs and MBVs. *N* = 3 biological replicates per condition. The EV amount was derived from the same number of donor cells. **(F)** Number of THP-1 monocytes per well that bound to HUVECs treated with CM-EVs or MBVs isolated from pNFs or from pCAFs silenced or not for THY1. HUVECs were treated with equal numbers of pNF- or pCAF-derived EVs. *N* = 3 biological replicates for pNF1 and pCAF1 and 5 biological replicates for pNF3 and pCAF3. Data are presented as means ± SEM. One-way ANOVA with Tukey's multiple comparison test for (B, C, E, F) and two-tailed Wilcoxon matched-pairs test for (D). All significant *P* values are included in the figure.

Fig. 6

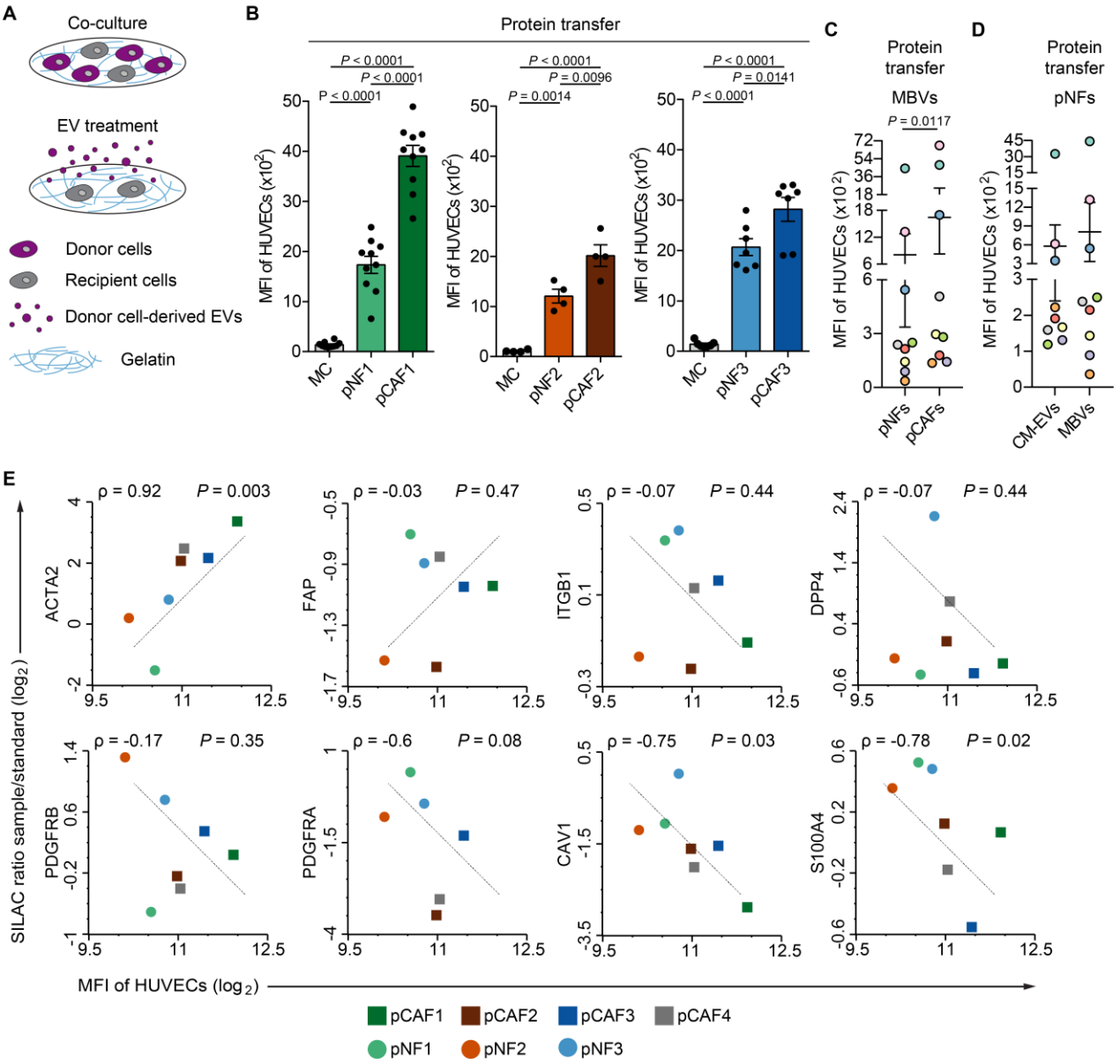

Fig. 6. CAFs have an enhanced protein transfer ability. (A) The direct co-culture method used in Fig. 6B. pNF- or pCAF-derived EVs were used to treat HUVECs in Fig. 6C-D. **(B)** Quantification of the protein transfer from pCAFs or pNFs to HUVECs. *N* = 10 biological replicates for pNF1 and pCAF1, 4 biological replicates for pNF2 and pCAF2, and 7 biological replicates for pNF3 and pCAF3. **(C)** Quantification of the amount of proteins transferred by pNF- and pCAF-derived MBVs to HUVECs. The EV amount was derived from the same number of donor cells. Colors indicate paired independent experiments. *N* = 9 biological replicates per cell line. Data are normalized to the MFI of the monoculture of HUVECs. The data related to pCAF-derived MBVs also are shown in Fig. 5D.

(D) Quantification of the amount of proteins transferred by pNF-derived CM-EVs and MBVs to HUVECs. The EV amount was derived from the same number of donor cells. Colors indicate the paired independent experiments. *N* = 9 biological replicates per EV type. Data are normalized to the MFI of the monoculture of HUVECs. The data related to pNF-derived MBVs also are shown in Fig. 6C. **(E)** Scatter plot showing the correlation between the abundance of CAF markers in fibroblasts (Data File S4) and the amount of proteins that they transferred to HUVECs, which corresponds to the data shown in fig. S5C. Data are in $\log_2$ scale (ρ, Spearman rank correlation). Data are presented as means ± SEM. One-way ANOVA with Tukey's multiple comparison test for (B) and two-tailed Wilcoxon matched-pairs test for (C, D). All significant *P* values are included in the figure.

Fig. 7

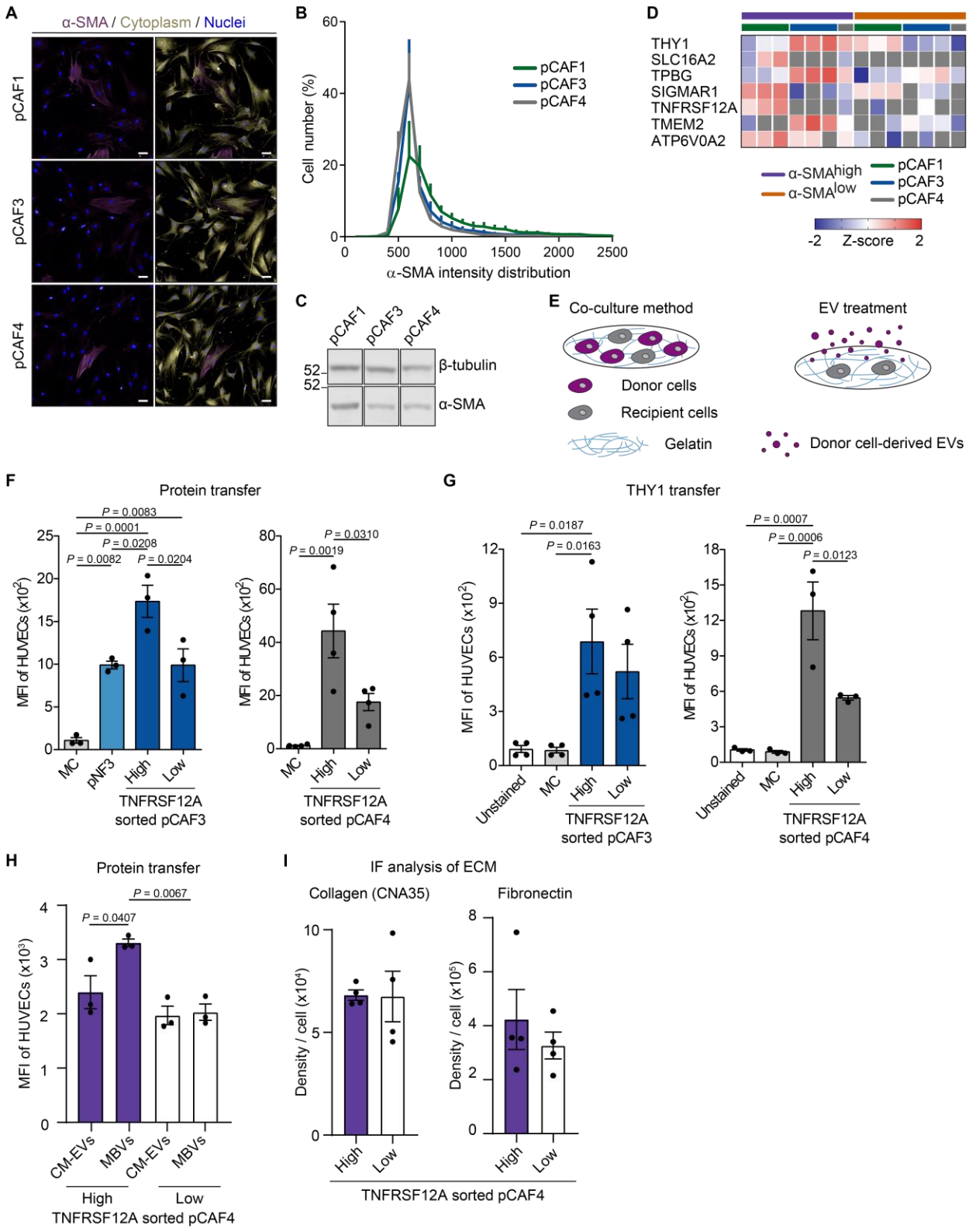

Fig. 7. CAFs with high protein transfer ability are α-SMA^{high} and TNFRSF12A^{high}. (A) Representative images (maximum intensity projection processing from confocal z-stack) of α-SMA staining in pCAFs. Cytoplasm and nuclei were stained with HCS CellMask and DAPI, respectively.

Scale bar = 50 µm. Representative of 4 sets of cells per cell line. **(B)** Frequency plot showing the percentage of pCAFs across the different values of α-SMA intensity from the analysis of α-SMA staining in (A). *N* = 4 biological replicates per cell line. Two-sample Kolmogorov-Smirnov test. **(C)** Representative Western blot showing α-SMA protein abundance in pCAFs. β-tubulin was used as loading control. Lanes are not contiguous but come from the same blot. Representative of 3 sets of cells per cell line. **(D)** Heatmap based on the Z-score of the LFQ intensity (log_2) of the cell surface proteins identified in pCAFs (subset of proteins from fig. S6C). *N* = 7 biological replicates for α-SMA^{high} and for α-SMA^{low} pCAFs. **(E)** The direct co-culture method used in Fig. 7F-G. EVs isolated from TNFRSF12A^{high} and TNFRSF12A^{low} pCAFs were used to treat HUVECs in Fig. 7H. **(F)** Quantification of the protein transfer from TNFRSF12A^{high} pCAFs, TNFRSF12A^{low} pCAFs or pNFs to HUVECs. *N* = 3 biological replicates for pNF3 and pCAF3, and 4 biological replicates for pCAF4. **(G)** Quantification of THY1 protein abundance in monoculture of HUVECs and HUVECs that were co-cultured with TNFRSF12A^{high} or TNFRSF12A^{low} pCAFs. *N* = 4 biological replicates for pCAF3 and 3 biological replicates for pCAF4. **(H)** Quantification of the amount of proteins transferred by TNFRSF12A^{high} pCAF- and TNFRSF12A^{low} pCAF-derived CM-EVs and MBVs to HUVECs. *N* = 3 biological replicates per condition. Data are normalized to the MFI of the monoculture. The EV amount was derived from the same number of donor cells. **(I)** Quantification of fibrillar collagen (CNA35) and fibronectin produced by TNFRSF12A^{high} and TNFRSF12A^{low} pCAFs. *N* = 4 biological replicates per condition. Data in (F, G, H, I) are presented as means ± SEM. One-way ANOVA with Tukey's multiple comparison test in (F, G, H) and two-tailed unpaired *t*-test with Welch's correction in (I). All significant *P* values are included in the figure.

Fig. 8

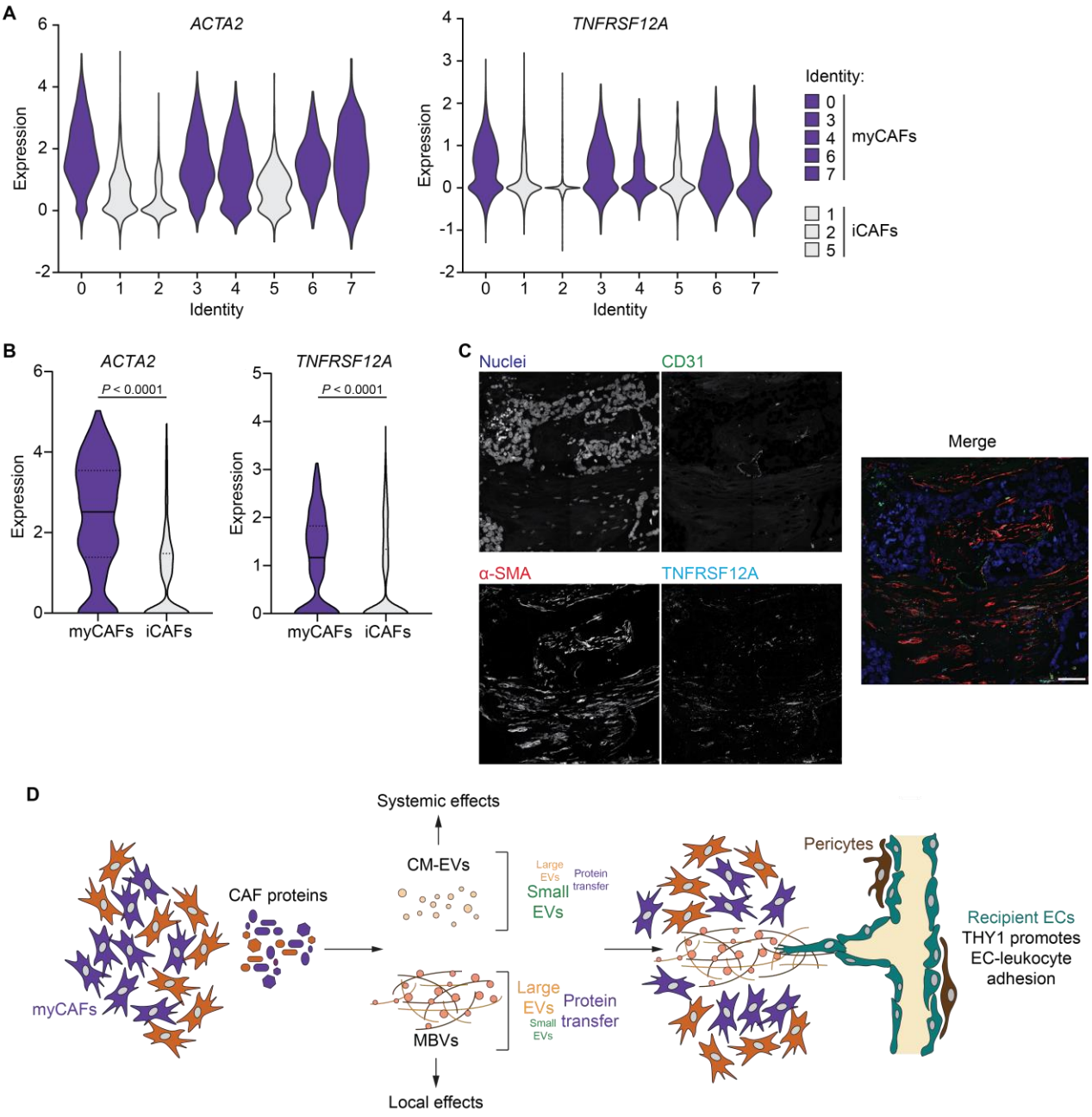

Fig. 8. Characterization of CAFs with high protein transfer ability. (A, B) Violin plot showing the expression of *ACTA2* and *TNFRSF12A* in myCAF and iCAF subpopulations. Data in (A) are from [16] and data in (B) are from [7]. Two-tailed Mann-Whitney U test. All significant *P* values are included in the figure. **(C)** Representative image of TNFRSF12A, α-SMA and CD31 staining in a tumor tissue section from a patient with breast cancer (maximum Z projection). Nuclei were stained with

Hoechst-33342. Scale bar = 50 µm. **(D)** Working model showing myCAF-EC communication based on MBV-mediated transfer of proteins.

fig. S1

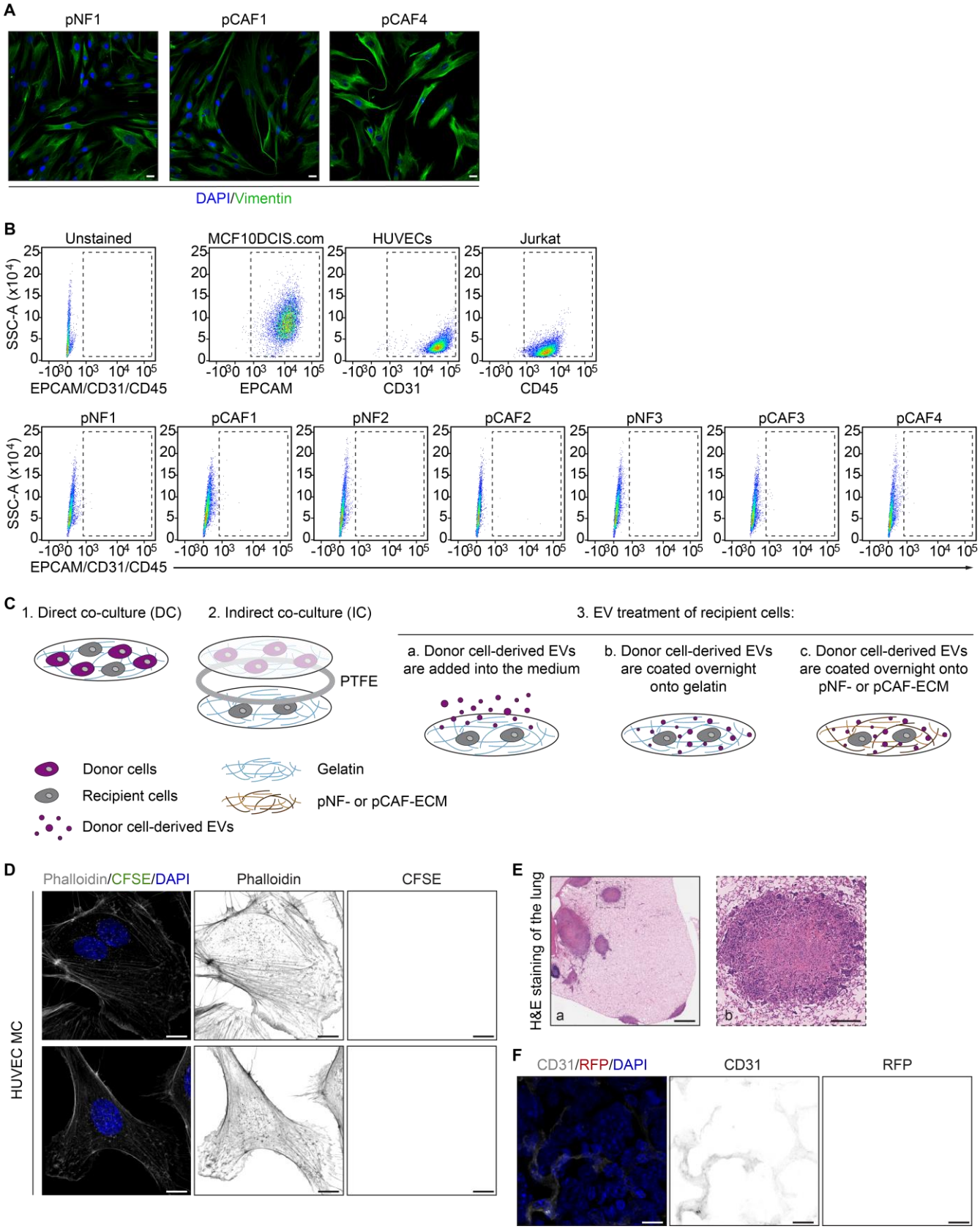

fig. S1. Fibroblast characterization, methods to measure the transfer of proteins and THY1, and control images for protein transfer in vitro and in vivo. (A) Representative images of vimentin staining in pNFs and pCAFs. Nuclei were stained with DAPI. Scale bar = 20 µm. Representative of 4 sets of cells per cell line. **(B)** Representative flow cytometry plots of unstained cells, MCF10DCIS.com cells stained for epithelial cell adhesion molecule (EPCAM), HUVECs stained for platelet endothelial cell adhesion molecule (PECAM1, commonly referred to as CD31), Jurkat cells stained for receptor-type tyrosine-protein phosphatase C (PTPRC, commonly referred to as CD45) and representative flow cytometry plots of pCAFs and pNFs stained for all the three PE-conjugated markers. The x-axis shows the fluorescence in the PE channel. Representative of 1 set of cells per cell line. **(C)** Schematic of the co-culturing methods and of the methods used to treat the recipient cells with donor cell-derived EVs used to study protein and THY1 transfer. **(D)** Representative images (maximum intensity projection processing from confocal z-stack) of HUVEC monoculture (MC, CFSE-unstained control: the acquisition setting for CFSE is the same as Fig. 1B). Actin and nuclei were stained with phalloidin and DAPI, respectively. Scale bar = 10 µm. Representative of 8 sets of cells. **(E)** Representative image of hematoxylin and eosin stained metastases in lung section, scale bar = 1 mm (a) and 200 µm (b). Representative of 7 mice. **(F)** Representative image (maximum intensity projection processing from confocal z-stack) of the tumor area in the lung of non-RFP expressing control mice stained for CD31. The acquisition setting in the RFP channel is the same as Fig. 1H-I. Nuclei were stained with DAPI. Scale bar = 10 µm. Representative of 2 mice.

fig. S2

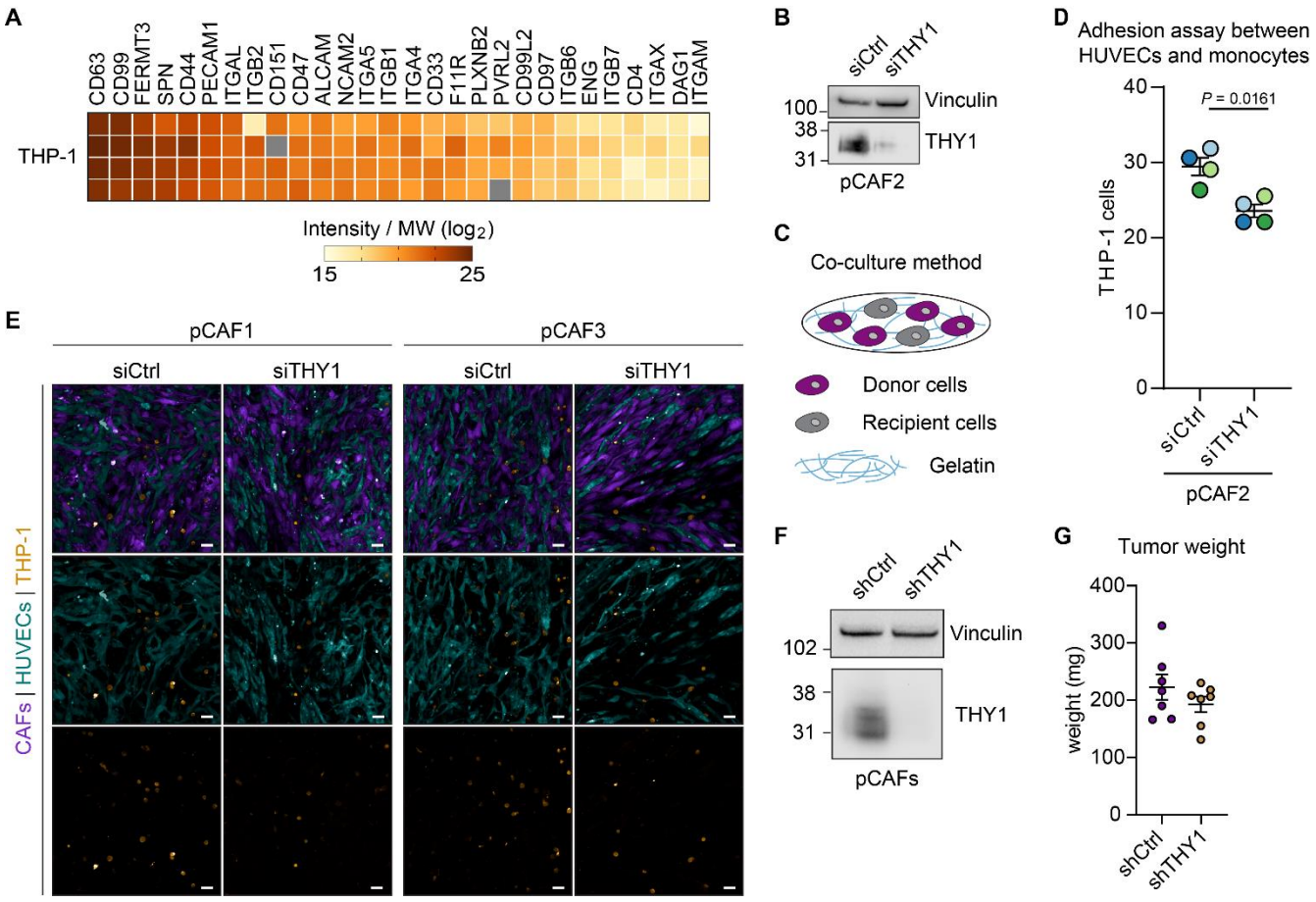

fig. S2. CAF-derived THY1 mediates monocyte adhesion to ECs. (A) Heatmap based on intensity value divided by the MW in the log_2 scale of the cell adhesion molecules that were identified in THP-1 monocytes. N = 4 biological replicates. THY1 binding partners are: ITGB2, ITGA5, ITGB1, CD97, ITGAX, ITGAM. **(B)** Representative Western blot showing THY1 protein abundance in pCAF2 transfected with siCtrl or siTHY1. Vinculin was used as loading control. **(C)** The direct co-culture method used in fig. S2D. **(D)** Number of THP-1 monocytes per field that bound to HUVECs co-cultured with pCAF2 silenced or not for THY1. Colors indicate paired independent experiments. N = 4 biological replicates per condition. **(E)** Representative images for the experiment in Fig. 3G showing the binding of THP-1 monocytes to HUVECs co-cultured with siCtrl or siTHY1 pCAFs. Scale bar = 50 µm. N = 4 biological replicates for pCAF1 and 3 biological replicates for pCAF3. **(F)** Representative Western blot showing THY1 protein abundance in shCtrl and shTHY1 pCAFs,

vinculin was used as loading control. **(G)** Tumor weight of 4T1 tumors co-transplanted with pCAF1 shCtrl/shTHY1. N = 7 mice per condition. Data are presented as means ± SEM. Two-tailed paired t-test for (D) and unpaired t-test with Welch's correction for (G). All significant *P* values are included in the figure.

fig. S3

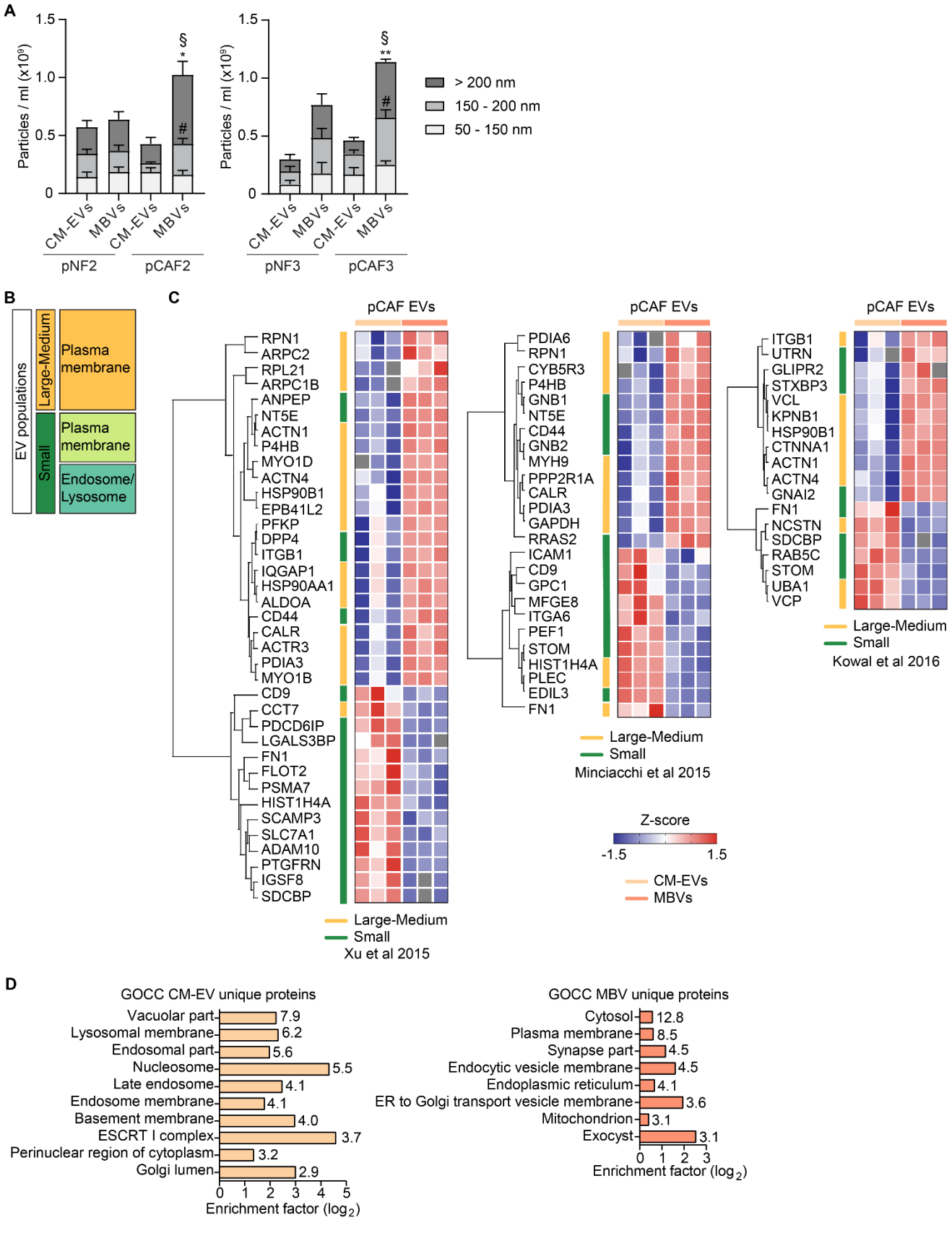
A
Particles / ml (x10⁹)
1.5
1.0
0.5
0
§
*
#
§
**
#
> 200 nm
150 - 200 nm
50 - 150 nm
CM-EVs
MBVs
CM-EVs
MBVs
pNF2
pCAF2
pNF3
pCAF3
B
EV populations
Large-Medium
Small
Plasma membrane
Plasma membrane
Endosome/ Lysosome
C
pCAF EVs
RPN1
ARPC2
RPL21
ARPC1B
ANPEP
NT5E
ACTN1
P4HB
MYO1D
ACTN4
HSP90B1
EPB41L2
PFKP
DPP4
ITGB1
IQGAP1
HSP90AA1
ALDOA
CD44
CALR
ACTR3
PDIA3
MYO1B
CD9
CCT7
PDCD6IP
LGALS3BP
FN1
FLOT2
PSMA7
HIST1H4A
SCAMP3
SLC7A1
ADAM10
PTGFRN
IGSF8
SDCBP
Large-Medium
Small
Xu et al 2015
pCAF EVs
PDIA6
RPN1
CYB5R3
P4HB
GNB1
NT5E
CD44
GNB2
MYH9
PPP2R1A
CALR
PDIA3
GAPDH
RRAS2
ICAM1
CD9
GPC1
MFGE8
ITGA6
PEF1
STOM
HIST1H4A
PLEC
EDIL3
FN1
Large-Medium
Small
Minciacchi et al 2015
Z-score
-1.5
1.5
CM-EVs
MBVs
pCAF EVs
ITGB1
UTRN
GLIPR2
STXBP3
VCL
KPNB1
HSP90B1
CTNNA1
ACTN1
ACTN4
GNAI2
FN1
NCSTN
SDCBP
RAB5C
STOM
UBA1
VCP
Large-Medium
Small
Kowal et al 2016
D
GOCC CM-EV unique proteins
Vacuolar part 7.9
Lysosomal membrane 6.2
Endosomal part 5.6
Nucleosome 5.5
Late endosome 4.1
Endosome membrane 4.1
Basement membrane 4.0
ESCRT I complex 3.7
Perinuclear region of cytoplasm 3.2
Golgi lumen 2.9
0 1 2 3 4 5
Enrichment factor (log2)
GOCC MBV unique proteins
Cytosol 12.8
Plasma membrane 8.5
Synapse part 4.5
Endocytic vesicle membrane 4.5
Endoplasmic reticulum 4.1
ER to Golgi transport vesicle membrane 3.6
Mitochondrion 3.1
Exocyst 3.1
0 1 2 3
Enrichment factor (log2)

fig. S3. Characterization of the EV populations. (A) Total amount and size distribution profile of the CM-EVs and MBVs secreted by pNF2 and pCAF2 (N = 4 biological replicates per condition) and pNF3 and pCAF3 (N = 3 biological replicates per condition) using nanoparticle tracking analysis. Data are presented as means ± SEM. pNF2/pCAF2 dataset: * $P \leq 0.05$ between pCAF2-derived MBVs and pCAF2-derived CM-EVs or pNF2-derived MBVs or pNF2-derived CM-EVs for the >200 nm fraction; # $P \leq 0.05$ between pCAF2-derived MBVs and CM-EVs for the 150–200 nm fraction; § $P \leq 0.05$ between the total amount of pCAF2-derived MBVs and pCAF2-derived CM-EVs or pNF2-derived CM-EVs. pNF3/pCAF3 dataset: ** $P \leq 0.01$ between pCAF3-derived MBVs and pCAF3-derived CM-EVs or pNF3-derived CM-EVs for the >200 nm fraction; # $P \leq 0.05$ between pCAF3-derived MBVs and pNF3-derived CM-EVs for the 150–200 nm fraction; § $P \leq 0.05$ between the total amount of pCAF3-derived MBVs and pCAF3-derived CM-EVs or pNF3-derived CM-EVs. *P* values were determined by one-way ANOVA with Tukey's multiple comparison test and all significant *P* values are included in the figure. **(B)** Schematic representing the different EV populations based on their size and subcellular origin. **(C)** Hierarchical clustering based on average Euclidean distance and heatmap based on the Z-score of the LFQ intensity (log_2) of the proteins with a significant fold change in abundance between CM-EVs and MBVs. $P < 0.05$ two-tailed *t*-test. N = 3 biological replicates per EV type. The colored bar in each heatmap integrates the information from a specific proteomic study [57, 58, 59] in which the different subpopulations of EVs as depicted in fig. S3B were investigated. **(D)** GOCC enrichment analysis of the proteins identified in CM-EVs or MBVs only, using the pCAF proteome (Data File S5) as reference (Fisher exact test). The terms are sorted by descending *P* (–Log) as indicated on the side of each bar. The terms that are generally associated with EVs (such as extracellular vesicular exosomes and extracellular membrane-bounded organelle) were not included. N = 3 biological replicates per EV type.

fig. S4

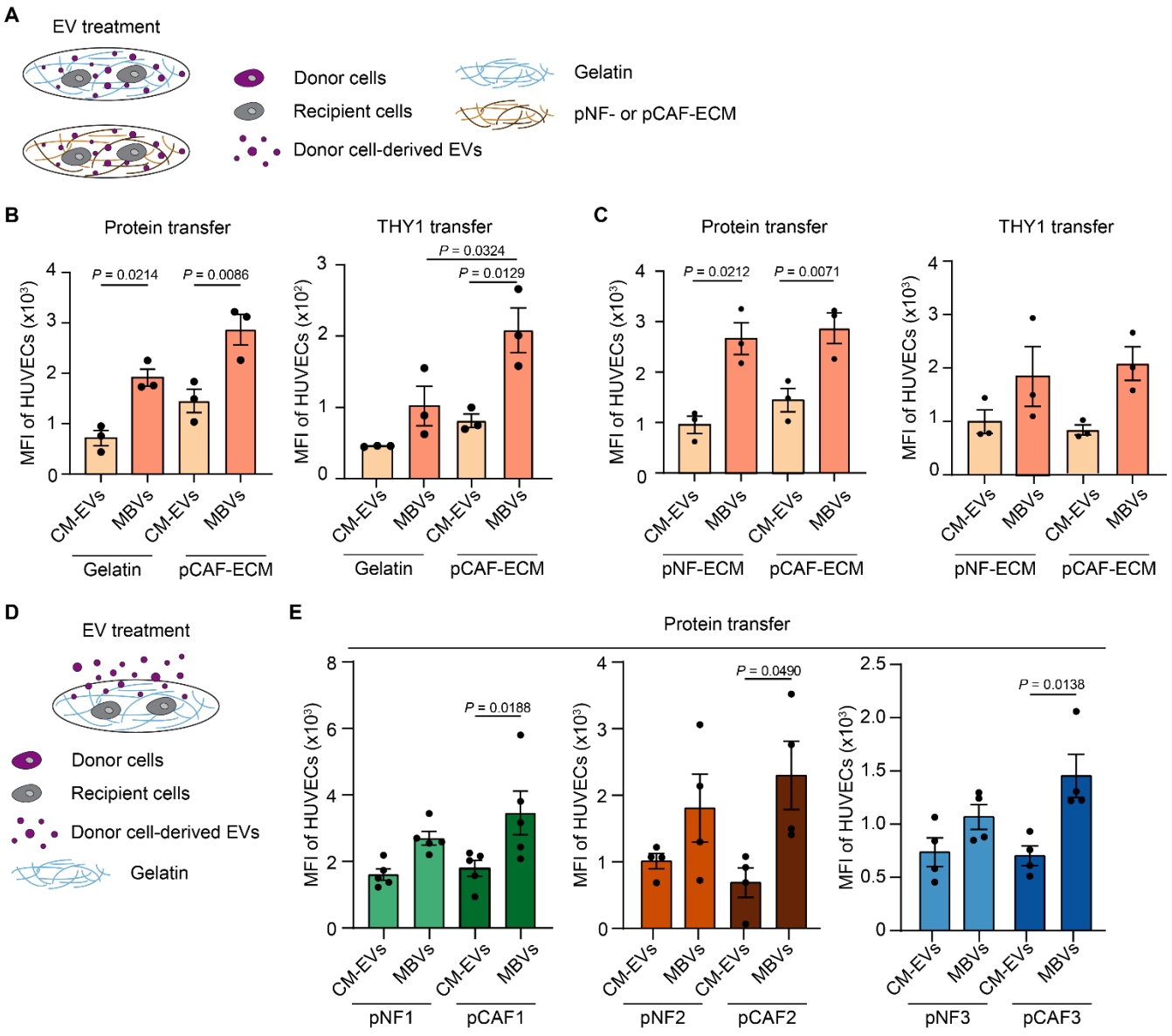

fig. S4. MBVs have an enhanced protein transfer ability compared to CM-EVs. (A) Method of EV treatment used to treat HUVECs in fig. S4B-C: pCAF-derived EVs were coated overnight either on gelatin or on fibroblast-derived matrix before HUVECs were plated on top. **(B)** Quantification of the amount of proteins and THY1 transferred by pCAF-derived CM-EVs and MBVs to HUVECs. The EV amount was derived from the same number of donor cells. EVs were coated on gelatin or pCAF-ECM. N = 3 biological replicates per condition. Data are normalized to the MFI of the monoculture of HUVECs. **(C)** Quantification of the amount of proteins and THY1 transferred by pCAF-derived CM-EVs and MBVs to HUVECs. The EV amount was derived from the same number of donor cells.

EVs were coated on pNF- or pCAF-ECM. N =3 biological replicates per condition. Data are normalized to the MFI of the monoculture of HUVECs. **(D)** Method of EV treatment used in fig. S4E: pNF- or pCAF-derived EVs were added to the HUVEC culture medium. **(E)** Quantification of the amount of proteins transferred by pNF- and pCAF-derived CM-EVs and MBVs to HUVECs. N = 5 biological replicates for pNF1 and pCAF1 and *N* = 4 biological replicates for pNF2 and pCAF2 and for pNF3 and pCAF3. HUVECs were treated with equal numbers of pNF- or pCAF-derived EVs. Data are normalized to the MFI of the monoculture of HUVECs. Data in (B, C, E) are presented as means ± SEM. *P* values were determined by one-way ANOVA with Tukey's multiple comparison test. All significant *P* values are included in the figure.

fig. S5

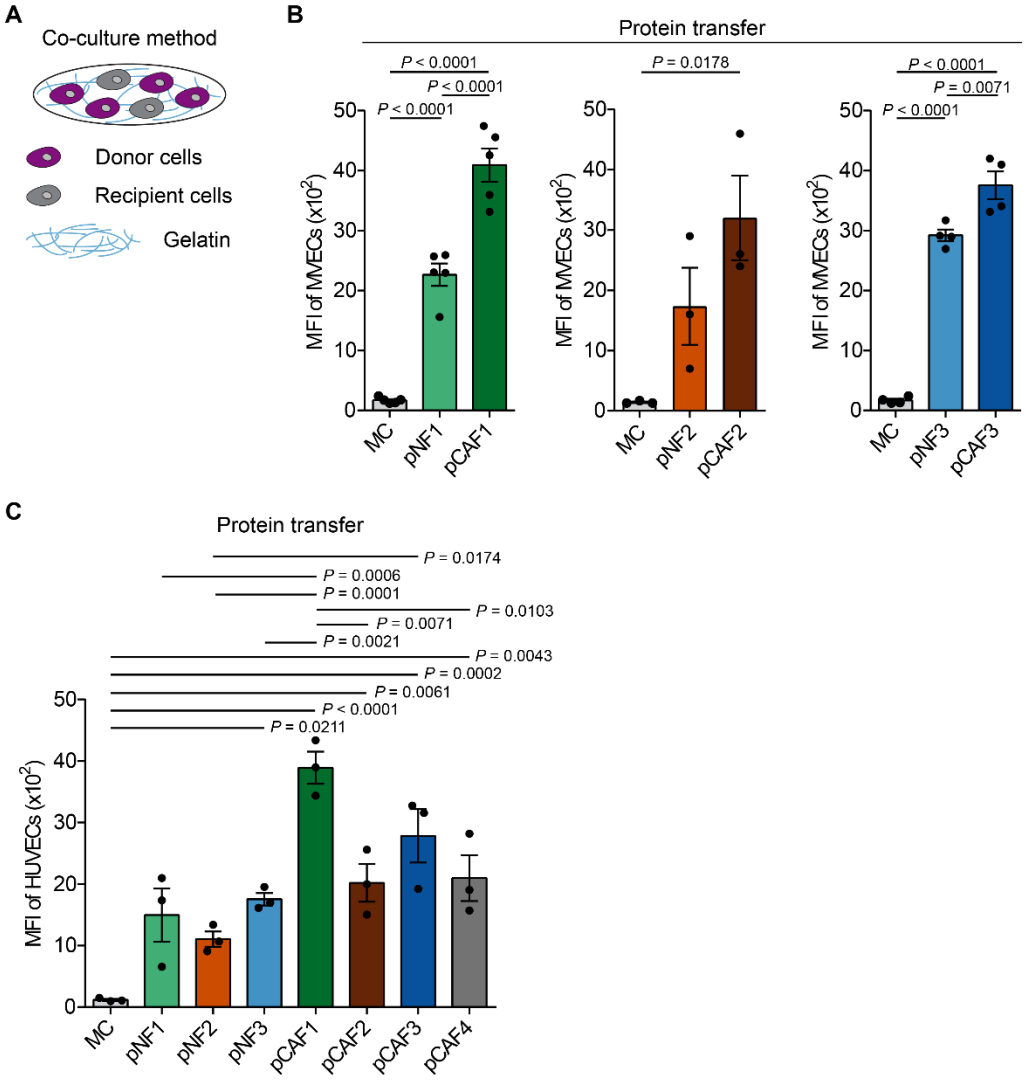

fig. S5. Quantification of the amount of proteins transferred from CAFs to either HUVECs or MVECs. (A) The direct co-culture used in fig. S5B-C. **(B)** Quantification of the protein transfer from pNFs or pCAFs to MVECs. *N* = 5 biological replicates for pNF1 and pCAF1, 3 biological replicates for pNF2 and pCAF2, and 4 biological replicates for pNF3 and pCAF3. **(C)** Quantification of the protein transfer from pNFs or pCAFs to HUVECs. N = 3 biological replicates per cell line (these data also are included in Fig. 6B). Data are presented as means ± SEM in (B, C). *P* values were determined by one-way ANOVA with Tukey's multiple comparison test. All significant *P* values are included in the figure.

fig. S6

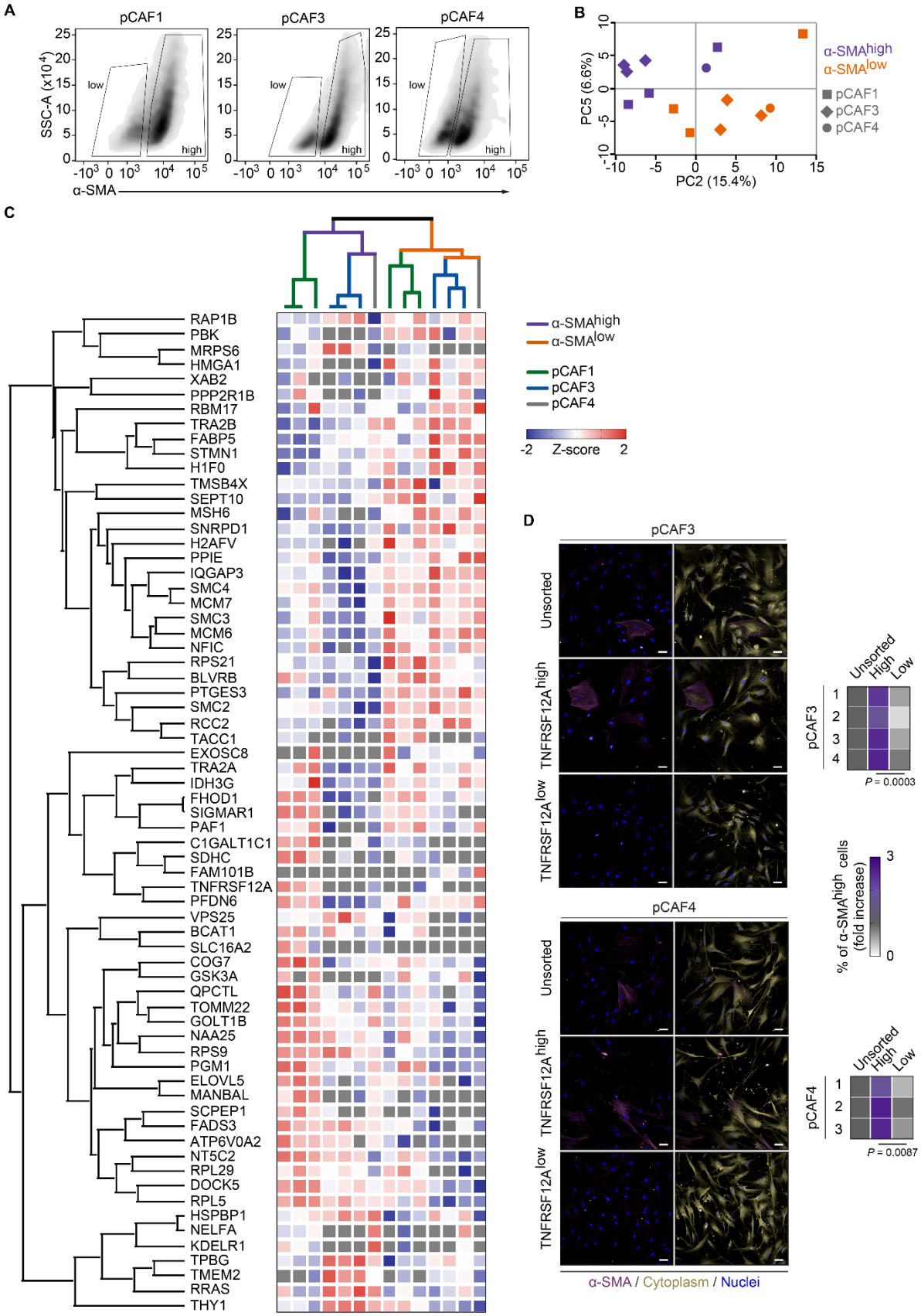
A
pCAF1
pCAF3
pCAF4
SSC-A (x10^4)
low
high
α-SMA
B
PC5 (6.6%)
PC2 (15.4%)
α-SMAhigh
α-SMAlow
pCAF1
pCAF3
pCAF4
C
RAP1B
PBK
MRPS6
HMGA1
XAB2
PPP2R1B
RBM17
TRA2B
FABP5
STMN1
H1F0
TMSB4X
SEPT10
MSH6
SNRPD1
H2AFV
PPIE
IQGAP3
SMC4
MCM7
SMC3
MCM6
NFIC
RPS21
BLVRB
PTGES3
SMC2
RCC2
TACC1
EXOSC8
TRA2A
IDH3G
FHOD1
SIGMAR1
PAF1
C1GALT1C1
SDHC
FAM101B
TNFRSF12A
PFDN6
VPS25
BCAT1
SLC16A2
COG7
GSK3A
QPCTL
TOMM22
GOLT1B
NAA25
RPS9
PGM1
ELOVL5
MANBAL
SCPEP1
FADS3
ATP6V0A2
NT5C2
RPL29
DOCK5
RPL5
HSPBP1
NELFA
KDELR1
TPBG
TMEM2
RRAS
THY1
α-SMAhigh
α-SMAlow
pCAF1
pCAF3
pCAF4
-2
Z-score
2
D
pCAF3
Unsorted
TNFRSF12Ahigh
TNFRSF12Alow
pCAF4
Unsorted
TNFRSF12Ahigh
TNFRSF12Alow
α-SMA / Cytoplasm / Nuclei
Unsorted
High
Low
pCAF3
P = 0.0003
% of α-SMAhigh cells (fold increase)
3
0
Unsorted
High
Low
pCAF4
P = 0.0087

1504

fig. S6. Characterization of the α-SMA^{high} and α-SMA^{low} subpopulations. (A) Gating strategy to sort the α-SMA^{low} and α-SMA^{high} subpopulations. **(B)** Principal component analysis based on 2,080 proteins identified across all the pCAF subpopulations. N =7 biological replicates for α-SMA^{low} and for α-SMA^{high} cell line. **(C)** Hierarchical clustering based on average Euclidean distance and heatmap based on the Z-score of the LFQ intensity (log_2) of the proteins with a fold change ≥ 1.5 and $P \leq 0.05$. N = 7 biological replicates for α-SMA^{low} and for α-SMA^{high} cell line. **(D)** Representative images (maximum intensity projection processing from confocal z-stack) of α-SMA staining in unsorted, TNFRSF12A^{high} and TNFRSF12A^{low} pCAFs. Cytoplasm and nuclei were stained with HCS CellMask and DAPI, respectively (scale bar = 50 µm). The heatmap shows the percentage of α-SMA^{high} pCAFs in the three populations. N = 4 biological replicates for pCAF3 and 3 biological replicates for pCAF4. *P* values were determined by two-tailed unpaired *t*-test with Welch's correction. All significant *P* values are included in the figure.

fig. S7

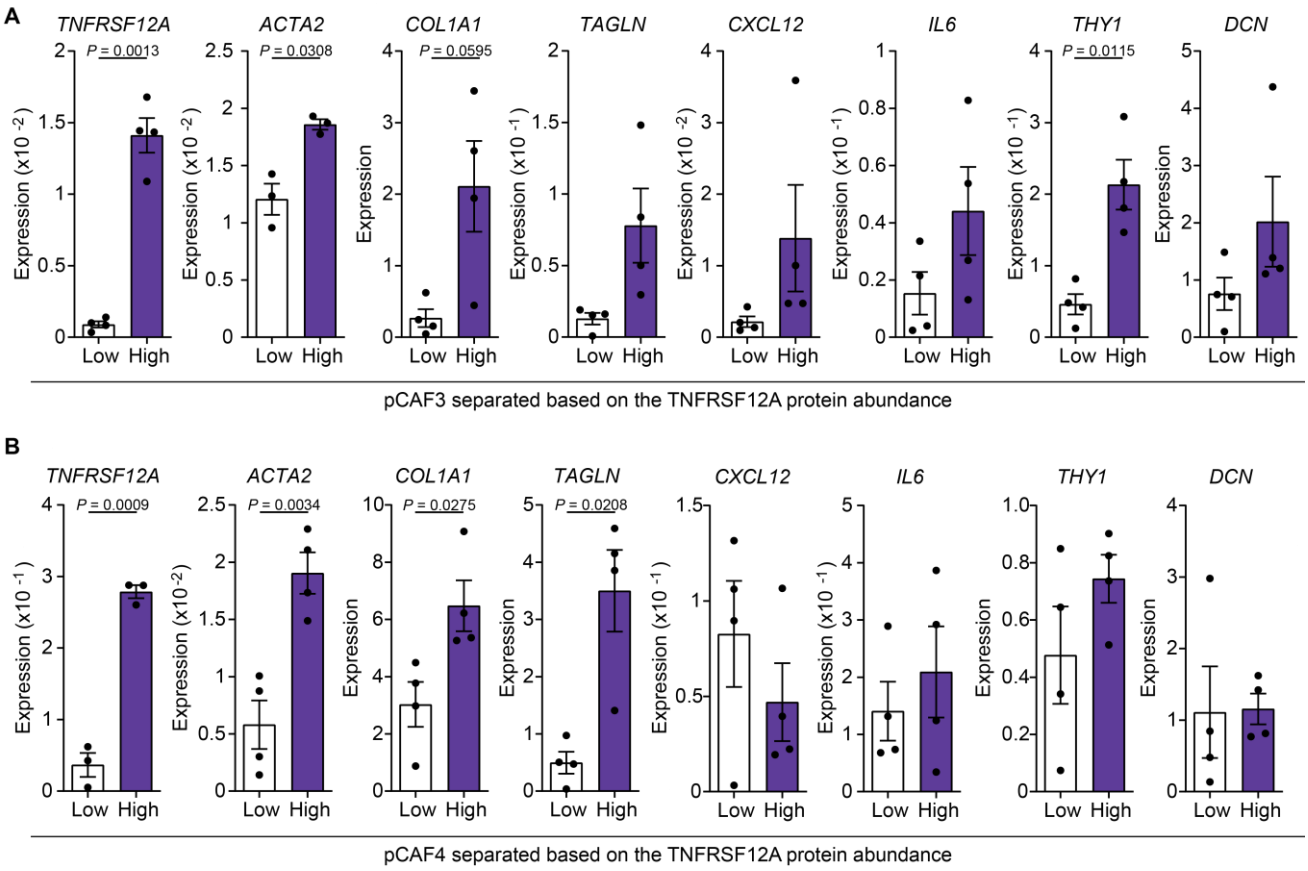

fig. S7. CAFs with enhanced protein transfer ability express myCAF markers. (A, B) mRNA expression of *TNFRSF12A*, *ACTA2*, *COL1A1*, *TAGLN*, *CXCL12*, *IL6*, *THY1*, *DCN* in pCAF3 (A) and pCAF4 (B) that were sorted based on TNFRSF12A protein amounts. The mRNA amount was normalized to *18S* expression. N =3 or 4 biological replicates per cell line**.** Data are presented as means ± SEM. *P* values were determined by two-tailed unpaired *t*-test with Welch's correction. All significant *P* values are included in the figure.

fig. S8

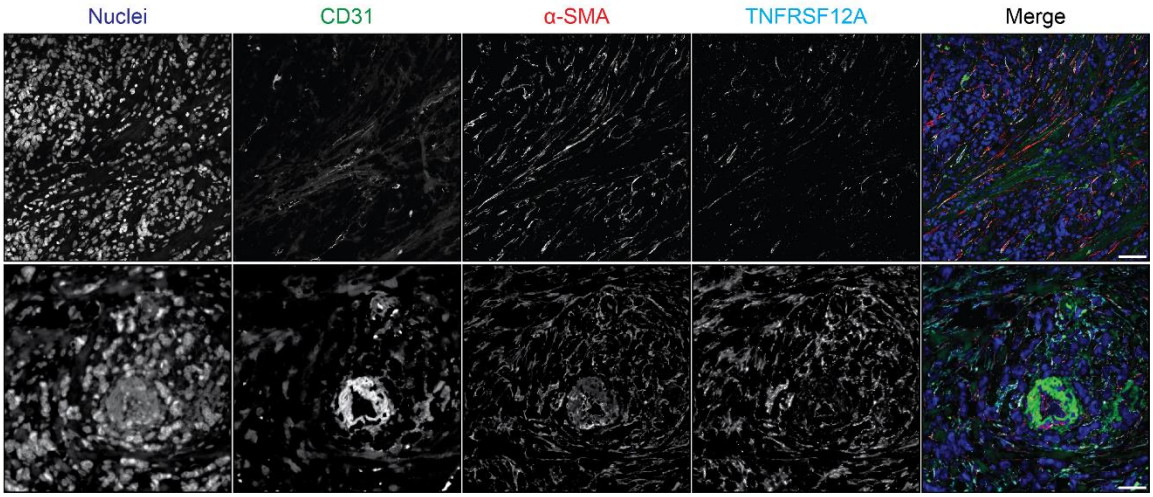

fig. S8. α-SMA$^+$ and TNFRSF12A$^+$ CAFs are present in breast cancer stroma. Representative images of tumor tissue sections from two patients with breast cancer stained for CD31, α-SMA and TNFRSF12A (maximum Z projection). Nuclei were stained with Hoechst-33342. Scale bar = 50 μm.

Table S1. List of primers used in the manuscript

Target	Forward	Reverse
TNFRSF12A	GAGAAGTTCACCACCCCCA	TGAATGAATGATGAGTGGGCGA
ACTA2	GTGTGCCCCTGAAGAGCAT	GCTGGGACATTGAAAGTCTCA
TAGLN1	GGTGGAGTGGATCATCGTGC	ATGTCAGTCTTGATGACCCCA
COL1A1	TGAAGGGACACAGAGGTTTCAG	GTAGCACCATCATTTCCACGA
THY1	AGAGACTTGGATGAGGAG	CTGAGAATGCTGGAGATG
IL6	GGTACATCCTCGACGGCATCT	GTGCCTCTTTGCTGCTTTCAC
CXCL12	CTACAGATGCCCATGCCGAT	CAGCCGGGCTACAATCTGAA
DCN	GGGCTGGCAGAGCATAAGTA	CAGAGCGCACGTAGACAT
18S	AGGAATTGACGGAAGGGCAC	GGACATCTAAGGGCATCACA

Data File S1. List of transferred proteins

Data File S2. THP-1 proteome

Data File S3. Proteome of pCAF-derived CM-EVs and MBVs

Data File S4. pCAF markers

Data File S5. Proteome of α-SMA^{high} and α-SMA^{low} pCAFs

Data File S6. Proteome of pCAFs